Received: 16 June 2021 | Revised: 24 August 2021 | Accepted: 10 September 2021

DOI: 10.1002/arp.1847

RESEARCH ARTICLE

WILEY

On-site non-destructive determination of the remanent magnetization of archaeological finds using field magnetometers

Tina Wunderlich[1,2] | Raphael Kahn[1,2] | Norbert R. Nowaczyk[3] | Natalie Pickartz[1,2] | Detlef Schulte-Kortnack[1,2] | Robert Hofmann[2,4] | Wolfgang Rabbel[1,2]

[1]Institute of Geosciences, Kiel University, Kiel, Germany

[2]Collaborative Research Center 1266, Kiel University, Kiel, Germany

[3]Helmholtz Centre Potsdam, GFZ German Research Centre for Geosciences, Potsdam, Germany

[4]Institute for Pre- and Protohistoric Archaeology, Kiel University, Kiel, Germany

Correspondence
Tina Wunderlich, Institute of Geosciences, Kiel University, Otto-Hahn-Platz 1, 24118 Kiel, Germany.
Email: tina.wunderlich@ifg.uni-kiel.de

Funding information
German Research Foundation, Grant/Award Numbers: Ho 5176/1, 290139

Abstract

The determination of the natural remanent magnetization (NRM) of archaeological features can be used for magnetic modelling, joining of shards, archaeomagnetic dating or the investigation of the firing–cooling–collapsing order of ancient buildings. The measurement of NRM is normally conducted on cylindrical or cubic samples in the laboratory. Nevertheless, archaeological finds should preferably not be destroyed, and laboratory instruments are high in costs. Therefore, we propose a lightweight and portable measurement set-up including already available field magnetometers (preferably caesium magnetometers) in which the archaeological sample of arbitrary shape, in our case a piece of daub, is mounted inside a gimbal to be rotated in all directions. The magnetic field of the sample is measured at a large number of rotational positions with the magnetometer kept at fixed position. In these measurements, the unknown direction of the NRM vector of the sample is rotated, whereas the average magnetic susceptibility of the sample and the ambient magnetic field are constant and known. Hence, the vector of NRM can be determined through least-squares inversion. For the inversion computation, the sample volume is discretized either as voxel model or approximated as an equivalent sphere. Under certain conditions depending on sample–sensor distance, dipole moment and radius of the sample, the approximation by a sphere is valid without effect on the accuracy of results. Empirically determined functions quantifying these conditions for different sensor sensitivities and noise levels are provided. Validation with laboratory measurements on palaeomagnetic subsamples from the destroyed daub samples indicate that the NRM can be determined by our proposed method with a maximum error in

inclination of 2°, in declination of 20° and in magnetization of ±0.6 A/m. This is accurate enough, for example, to determine from daub pieces of burnt house remains whether the building was burnt and cooled before or after it collapsed.

KEYWORDS
archaeology, linear inversion, magnetic modelling, remanent magnetization, susceptibility

1 | INTRODUCTION

Gradiometry or total field measurements are frequently applied for magnetic investigations of archaeological sites (Becker, 1995; Bis et al., 2021; Linford et al., 2007; Miller et al., 2019; Pickartz et al., 2019; Wilken et al., 2015). The map of magnetic anomalies is then understood as an image showing magnetic imprints of different archaeological features, for example, ditches, pits or walls, and enabling a determination of their location and approximate size. However, with this interpretation alone, the potential of magnetic investigations at archaeological sites is not fully explored, because only the resulting magnetic anomalies are determined but not their causative physical properties: the induced and remanent magnetization. The first depends on magnetic susceptibility and the ambient magnetic field, whereas the latter is the magnetization that is also present for some materials in absence of an external magnetic field.

The determination of the remanent portion of magnetization is important for the archaeological interpretation of magnetic anomalies for several reasons: (1) The assumption of a solely induced magnetization often used in the magnetic modelling of measured magnetic anomalies can lead to wrong estimations of source geometry and position (Clark, 2014); (2) accurately determined intensity and direction of a remanent magnetization can be used for dating, if palaeomagnetic reference records are available for the investigated site (Guerrero et al., 2015; Herries, 2009); (3) the Koenigsberger ratio, which is the ratio of remanent to induced magnetization strengths, can provide some first information about the magnetic mineralogy and related soil processes (Clark, 2014); and (4) the temporal order of subsequent thermoremanent magnetization (TRM) events and the pre- or post-cooling time point of the collapse of a burnt building can be determined (Shaffer, 1993).

For the accurate determination of the intensity and direction of the natural remanent magnetization (NRM), standard procedures exist where oriented samples are taken in the field and analysed in the laboratory. Different laboratory methods are available for the determination of the intensity and direction of the NRM as well as for further measurements, for example, the elimination of viscous remanent magnetization (VRM) components leading to the separation of the characteristic remanent magnetization (ChRM).

These standard laboratory analyses can be restricted for archaeological artefacts in following ways: Frequently, it is undesirable to destroy archaeological finds, which is necessary for most laboratory measurements using prisms, cylinders or pulverized samples. In some countries, the export of archaeological samples is prohibited, which may disable laboratory measurements for which no facilities exist inland. Another limiting factor may be the high costs for sensitive laboratory equipment but also for adequate rooms for its permanent installation. Therefore, it appears desirable to develop movable equipment, which can be brought to an excavation site or storage location of archaeological artefacts to perform the measurements on-site, even if this would be paid by a certain, but tolerable, loss in the accuracy of results.

With this background, we present a self-built, lightweight and portable measurement set-up using caesium field magnetometers and a numerical inversion scheme to non-destructively determine the NRM of archaeological finds.

The aims of this study are:

1. to develop, build and test a portable device for the non-destructive determination of the NRM of irregularly formed archaeological finds, which requires no extra laboratory-based equipment;
2. to develop a measurement and inversion procedure, which is as efficient as possible, but accurate enough for a reliable determination of the intensity and the strength of NRM;
3. to validate the results with remanent magnetization measurements performed on archaeomagnetic subsamples (thus destroying the archaeological sample) in a palaeomagnetic laboratory using the normally applied methods; and
4. to give recommendations for improvements towards a routinely applied determination of the NRM with the device presented here.

As an application example, we present measurements on burnt Neolithic house remains enabling to decide by means of NRM if the house, from which the samples were taken, cooled upright or after collapse.

2 | MATERIAL AND METHODS

The general concept of the measurement procedure presented here is to use an archaeological sample in its original shape, place it into a non-magnetic box, which is mounted inside a gimbal consisting of three frames and which can be rotated in all directions with the centrepoint of the sample staying at the same place. The gimbaled sample is then rotated stepwise in x- and y-direction, and the resulting anomalous magnetic field is measured with a magnetometer. A second magnetometer placed at larger distance from the sample is used for the correction of the temporal variations of the geomagnetic field.

The rotation of the sample also rotates the remanent magnetization vector, which is fixed with respect to the sample orientation. In contrast, the induced magnetization vector remains in the same direction despite sample rotation. However, the induced magnetic field anomaly of the sample may change, too, if its shape is non-spherical. Also, temporal variations of the ambient magnetic field may influence the induced magnetization, but usually to a minor extent. These assumptions will be validated later in Section 3. The anomalous field values for different sample orientations are then used to invert for the remanent magnetization. We found fixing the sensor position and rotating the sample, and thus the remanent magnetization vector, easier to put into practice than the reverse because the samples are small compared to the sensor of the field magnetometer.

2.1 | Measurement of the magnetic total field anomaly of the samples

The gimbal is built from frames of aluminium poles connected with plastic screws. The cardboard box containing the sample is mounted with tension belts with plastic buckles inside the gimbal frame. The gimbal itself is positioned on four plastic boxes, which are also used to fix a PE pole with the sensor of a caesium total field magnetometer (Figure 1: sensor 2; Cs-823B from Geometrics) at horizontal and vertical distances of each 0.245 m to the midpoint of the sample. In this position, the sample is in the sensitive zone of the magnetometer (Geometrics, 2004). For reference, a second magnetometer (Sensor 1) of the same type is placed 1.425 m horizontally apart from the sample, which is far enough away to be not influenced by the magnetic field of the sample. Additionally, with this set-up, the sample is placed in the horizontal dead zone, that is, the insensitive zone, of the reference magnetometer. The rotational angles of the gimbal are measured with protractors. All materials used are non-magnetic and lightweight. They can be found in a hardware store or can be replaced by, for example, wooden alternatives.

We used a compass to determine the orientation of the axis from the sample to the magnetometers with respect to magnetic north. This axis is defined as the *x*-direction of the Cartesian coordinate system used later on, whereas the *y*-axis is pointing towards east and the *z*-axis downwards.

For minimizing anthropogenic magnetic noise but still being sheltered from the weather, we performed the measurements in a wooden building at night-time. For this purpose, we used the Great Assembly hall of the rebuilt Viking Age village of Haithabu (northern Germany). The hall is completely built from wood and reed, and thus, no disturbing influences were observed (average field intensity at the second [reference] magnetometer was 50059.0 nT with a standard deviation of ±2.5 nT). During the measurement period, field models predict a magnetic field of ∼50 063 nT with an inclination of 69.13° and a declination of 3.2° (NOAA, 2021).

Before the measurements on the sample, the effect of the gimbal and the set-up itself were determined with both magnetometers using an empty cardboard box that was rotated into all 64 positions. By subtracting the reading of Sensor 1 from Sensor 2, temporal variations were eliminated resulting in $\Delta B_{Background}$.

After placing the sample box in the gimbal, the gimbaled box was rotated in steps of 45° counterclockwise around the *y*-axis. For each rotation step, measurements of the total magnetic field were taken with both magnetometers for 10 s using a sampling frequency of 10 Hz. Then, the box was rotated counterclockwise 45° around the *x*-axis, and again, eight positions with a step size of 45° around the *y*-axis were taken. This was repeated eight times yielding a total of

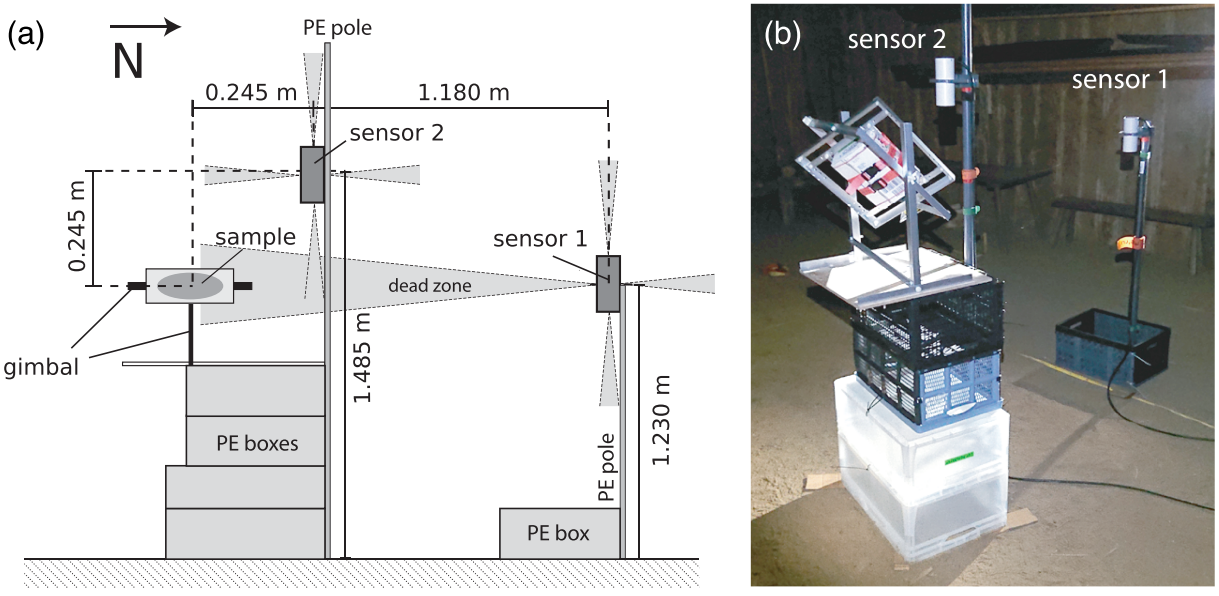

FIGURE 1 (a) Sketch of the measurement set-up with the gimbaled sample and two magnetometers (Sensors 1 and 2) mounted on PE poles. The insensitive zones (dead zones) of the sensors are marked with grey triangles. (b) Photography of the set-up inside the Viking Age Great Assembly hall [Colour figure can be viewed at wileyonlinelibrary.com]

64 different sample orientations. Measurement positions can be found in the appendix (Table A1). The complete measurement procedure took about 1 h and 20 min per sample.

The processing of the measured total field values consisted of (1) the correction for temporal variations by subtracting the reading of Sensor 1 from Sensor 2 for each time point, (2) subtracting the background effect $\Delta B_{Background}$ from these values and (3) determining the mean and standard deviation of measurements for each sample orientation. The residuals, termed ΔB_{obs} in the following, are the input for the inversion computation.

2.2 | Photogrammetric modelling of the samples

The samples used for this study originate from a burnt building at the archaeological site Makaranda on the Borđoš Plain near Novi Bečej in the Serbian Vojvodina, which was partly excavated in the frame of a Serbian–German cooperation in 2017. This site is a small hamlet consisting of only a few houses with Vinča and Tisza ceramic styles in the catchment of the central settlement of Borđoš (Hofmann et al., 2019; Medović et al., 2014). The settlement has been dated between 5 200 and 4 840 BCE by means of the ^{14}C method (two datings). Five daub pieces from the building were taken, marking the orientation towards magnetic north on their surface, whereas the angle to the horizontal plane was not marked.

On open research question is if the building was destroyed before firing or collapsed afterwards. Because the investigations presented in this paper can be used to determine the sequence of firing and collapse of a building, they can contribute to the archaeological discussion on the meaning of burnt houses in the past. Whereas some researchers suspect a practice of intentional 'closing' of houses behind the numerous burnt prehistoric buildings, others assume unintentional fires due to carelessness or burning for constructive reasons (e.g. Brami, 2017; Johnston et al., 2019).

In order to model the magnetic field of the samples accurately, the exact shape of the daub samples had to be determined. Therefore, photogrammetric modelling was performed. Several small adhesive points were placed on the daub samples in approx. 45° angular distance to allow for comparison of photographs and triangulation into a three-dimensional (3D) point cloud. For each sample, approx. 100 pictures were taken from all sides with a Nikon D750 camera with 60 mm lens and an aperture of 25, although the sample was placed on a white paper with constant illumination. Black marker points on the paper allowed for assigning a local coordinate system. As magnetic north was marked on the upper surface of the daub samples during collection, the coordinate system could be aligned easily with this orientation.

For the point cloud generation and digitization of the object, we used AgiSoft PhotoScan Pro. Further processing such as point cloud filtering, rendering and surface reconstruction was conducted with the programs CloudCompare (Version 2.10.1, 2019, GPL Software) and MeshLab 1.3.2 (Cignoni et al., 2008). The triangulated digital model was then discretized in voxels of 2.5 mm or 5 mm edge length. These data were used for volume determination of the daub sample and determining a representative sphere of the same volume (Figure 2).

All five samples have approximately the same dimensions and volumes in the range 279–522 cm^3. The aspect ratios and dimensions together with volume and radius of the equivalent sphere are listed in Table 1.

2.3 | Magnetic susceptibility of the samples

For reducing the degrees of freedom in computing the remanent magnetization, we determined the magnetic susceptibility through measurements beforehand. The measurements were performed on the surface of each sample with a Bartington MS2-K sensor that was calibrated before on a standard sample. For obtaining representative values, we measured multiply at several points on the surface, corrected for possible instrument drift and calculated the median, mean and standard deviations.

2.4 | Determination of remanent magnetization

The NRM is the remanent magnetization of a material composed of stable and viscous magnetic components. The stable component is the ChRM, which was gained during formation of the rock or of an archaeological artefact. Often, it is superimposed by an unstable component, the VRM, which is successively gained by being exposed to the varying magnetic field until sampling measurement. The VRM is acquired and lost logarithmically with time and hence mainly over hours to days (Gapeev et al., 1991). Thus, the VRM direction is not necessarily the same as the ChRM direction acquired during formation of the rock. The stable component of the NRM can be of various origin, for example, a TRM, which is acquired during cooling below the Curie temperature, a depositional remanent magnetization (DRM) in sediments, which is acquired through parallel alignment of magnetic particles to the geomagnetic field during deposition and subsequent fixation by the compacting sediment matrix, or a chemical remanent magnetization (CRM), which is acquired when magnetic minerals get precipitated by chemical processes such as oxidation and reduction.

With the measurement procedure described in this paper, we are neither able to differentiate between the different forms of NRM nor to separate the effect of VRM. Thus, we are aiming at determining the three components of the NRM vector of the samples by an inversion of the measured magnetic total field values for different rotations of the sample. To achieve this, two different geometrical approximations of the sample are used: (1) an approximation by voxels of different edge lengths and (2) a sphere with the same volume. We set up the formulae in a Cartesian coordinate system tied to the sample, in which the unknown NRM vector components are constants, whereas sensor position and induced magnetization vector components are variable but known.

The formulae for the inversion problem using a voxel model are given in Appendix A.1 and for the spherical model in Appendix A.2.

2.4.1 | Different inversion approaches

For each of the five daub samples, measurements for 64 different orientations were made. To evaluate (1) how many measurements are needed for sufficiently accurate determination of the remanent magnetization and (2) how the sample needs to be represented geometrically, we performed comparative test computations using the subsets of data listed in Table 2 (cf. also Table A1 in the appendix to see the orientations used for the reduced sets of measurements). The reduced datasets sample the whole sphere of orientations but at lower density (Figure 3).

2.5 | Validation measurements

To validate the NRM values obtained through the new approach, we determined the remanent magnetization and the magnetic susceptibility of the daub samples by well-established procedures in the

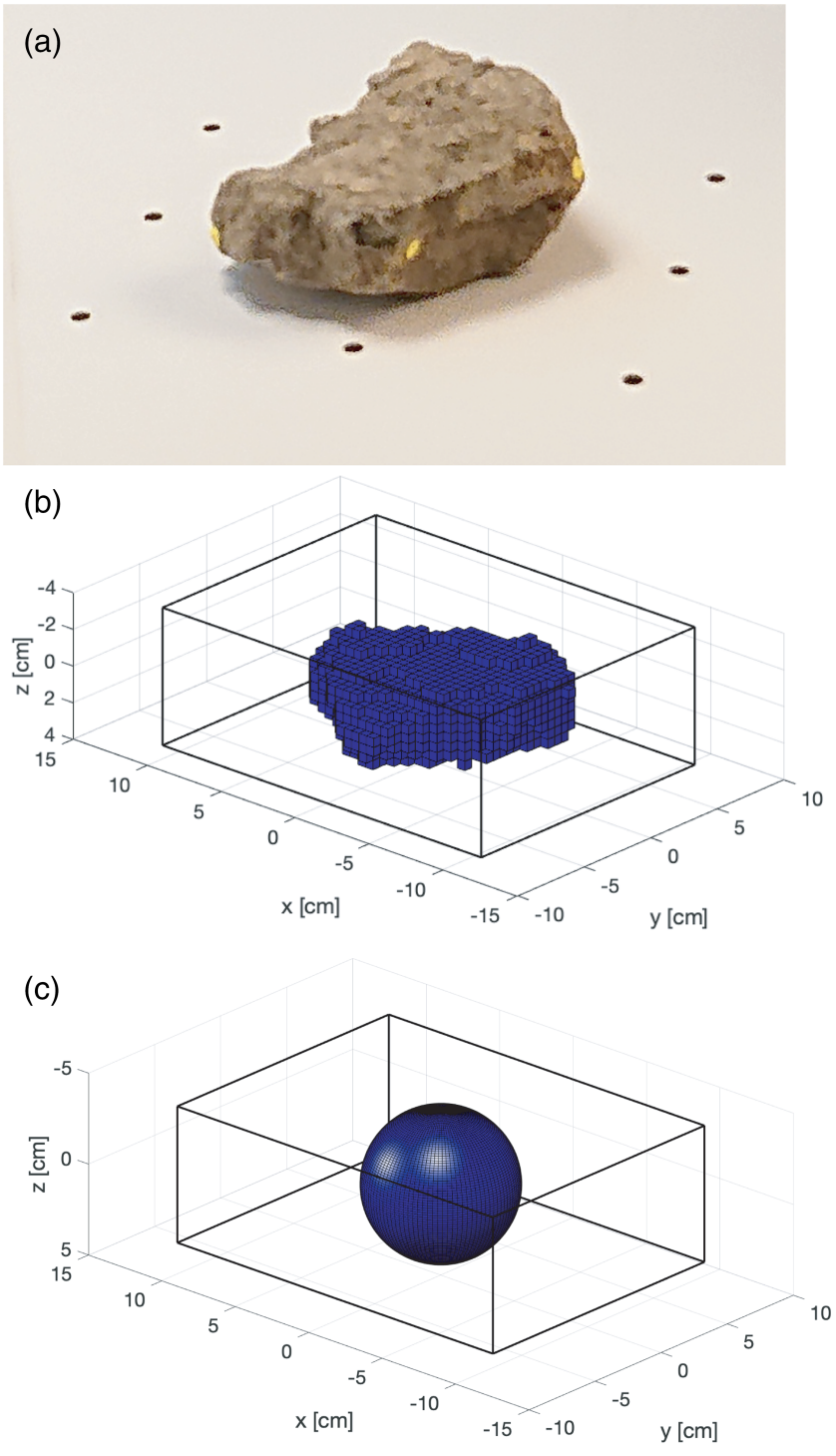

FIGURE 2 (a) Photo of sample 10071 on white paper with markers, (b) discretization of the sample with voxels of edge length 5 mm and (c) approximation of the sample by a sphere with the same volume as the triangulated object. The surrounding box marks the dimension of the cardboard box [Colour figure can be viewed at wileyonlinelibrary.com]

TABLE 1 List of aspect ratios, maximum length, volume and radius of the equivalent sphere for all samples

Sample	Aspect ratio *x*–*y*–*z*	Maximum length of sample (cm)	Volume (cm^3)	Mass (kg)	Density (kg/m^3)	Radius of equivalent sphere (cm)
10067	1–1–0.42	13.0	410.3	0.5985	1458.59	4.61
10070	1–0.89–0.46	14.0	521.9	0.6245	1196.54	4.99
10071	1–0.84–0.36	12.5	283.4	0.4275	1508.52	4.07
10072	0.90–1–0.34	14.5	480.6	0.6825	1420.03	4.86
10073	1–0.9–0.7	10.0	279.0	0.4565	1636.12	4.05

TABLE 2 Different number of measurement points and geometrical approximations of the sample that have been tested. All combinations of these categories have been evaluated, resulting in nine inversion approaches and results. For some samples the maximum number of measurement positions is 63 only due to measurement errors at one position

Number of measurement points	Geometrical approximation of the sample
64 (63)	Voxels of edge length 5 mm
22 (21)	Voxels of edge length 2.5 mm
6	Sphere with the same volume as triangulated model

palaeomagnetic laboratory at the Helmholtz Center Potsdam. The results of these methods are also used to verify or falsify the simplifying assumptions underlying the new approach.

For the laboratory measurements, the archaeological samples had to be cut into several specimen, cubes of 20 × 20 × 18 mm size while preserving the marking of the north orientation. To determine also a standard deviation and to investigate a possible inhomogeneity of the samples, for each sample, four to seven cubes were prepared and measured, originating from the inner and outer parts of the sample.

2.5.1 | Magnetic susceptibility

In a first step, the anisotropy of the magnetic susceptibility was measured on these prepared cubic samples using a calibrated AGICO Multi-Function Kappabridge MFK-1S with an alternating magnetic field of 976 Hz and an intensity of 200 A/m. The applied AGICO software (Saphyr 6) supplied the orientation angles and the normalized lengths of the principal anisotropy axes K_{max}, K_{int} and K_{min} as well as the bulk susceptibility.

2.5.2 | NRM and ChRM

In a next step, the direction and intensity of the NRM of the cubes were determined using a superconducting 2G Enterprises 755-4K SRM cryogenic magnetometer. The demagnetization was conducted in steps of 5, 10, 15, 20, 30, 40, 50, 65, 80 and 100 mT. The direction of the ChRM was determined via principal component analysis based on the procedure described in Kirschvink (1980). We determined the mean of all cubes and calculated the 95% confidence ellipse (α_{95}) according to Fisher (1953).

3 | RESULTS

In this section, we will first present the results of the magnetic susceptibility measurements using both surface sensor and laboratory equipment, because they are needed as input for the inversions. Second, we present the results on remanent magnetization obtained from all variants of the new approaches including a modelling study to review underlying assumptions, and third, we show and compare the results of the validation measurements.

3.1 | Magnetic susceptibility

3.1.1 | Surface magnetic susceptibility

The susceptibility values measured with the Bartington MS2-K sensor were determined at about 20 surface points on each sample. The mean and median susceptibility values of the samples and their standard deviation are listed in Table 3. For the inversion calculation, we used the median values. The median susceptibility values vary between 5.4 and 7.5 × 10^{-3} SI units and show a standard deviation of ±15%–30%. This variation is caused by the surface roughness, which leads to some variation in sensor coupling. For example, for a roughness of 3 mm depth, which was present on the samples, the response is reduced by 50% (Bartington, n.d.). The median mass susceptibility is in the range also found by Jordanova et al. (2018) for brown-coloured daub samples from Neolithic houses at Mursalevo-Deveboaz, Bulgaria.

3.1.2 | Magnetic susceptibility measured in laboratory

The results from the laboratory susceptibility measurements are twofold: The normalized principal axes of the AMS ellipsoid for all samples are shown in Figure 4a. All samples are characterized by comparable shapes of a slightly flattened ellipsoid. Thus, we can assume a (nearly)

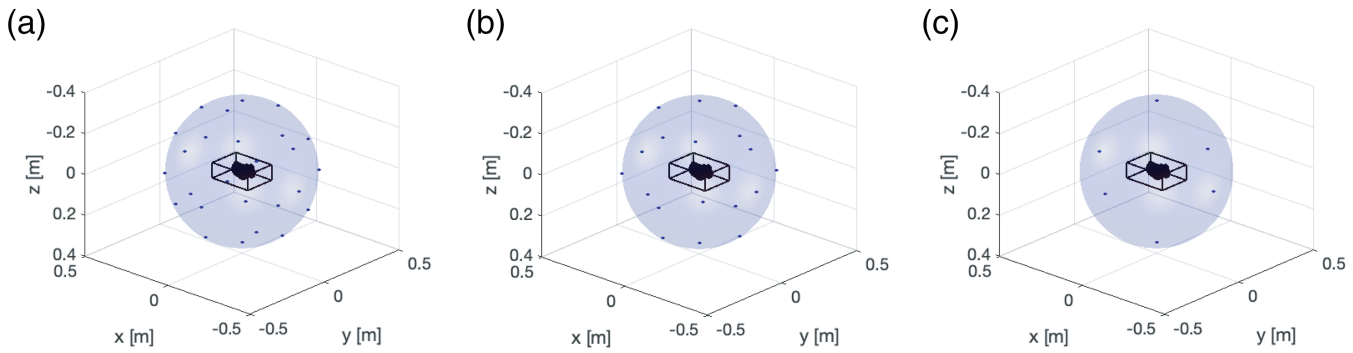

FIGURE 3 Sketches showing the distribution of sensor points around the sample for the complete ((a) 64 points) and reduced datasets ((b) 22 points and (c) 6 points). All measurement points lie on a virtual sphere around the midpoint of the sample [Colour figure can be viewed at wileyonlinelibrary.com]

isotropic magnetic susceptibility in the samples. In addition, susceptibilities measured on subsamples from the inner and outer part of the daub samples show the same values with magnitudes between approx. 600e-5 and 2000e-5 SI (Figure 4b). Compared with the surface susceptibility measurements, the laboratory values are 22%–158% higher, which is probably due to the bad coupling of the surface sensor. We assume the laboratory measurements to be 'true' but nevertheless use the surface measurements as input for the inversion, because for new measurements we normally only have the surface sensor.

3.2 | Remanent magnetization from magnetic field inversion

For each measurement position, the mean and standard deviation for all measurements over 10 s were determined. The standard deviation of 90% of the repeat measurements was <5%, corresponding to ±0.1 nT. Due to the regular advance of sample rotation, the measured amplitudes show a sinusoidal curve for each sample (e.g. sample 10067 in Figure 5a). The modelled field values for both voxel models are very similar and overlap in most points exactly (maximum <0.1%). The modelled values for the spherical geometry are slightly different (maximum <5% compared with the voxel model with 5 mm edge length). Generally, they fit well with the observed data points with a root mean square (RMS) error of 0.32 nT (∼7.6%). The curves show a small constant offset between their mean values (pink and black horizontal lines), which can be caused by several reasons:

1. Although the offset is constant for each sample, it is different for different samples ranging from 0.18 to 0.59 nT. The samples were measured at the same position in the Great Assembly hall, but nevertheless, we cannot exclude small changes in the surrounding of the measurement set-up, for example, variation of cables, that might lead to these small offsets.
2. If we exclude effects originating from the surrounding and because the offset is different for different samples, it might be the effect of VRM, which is not explicitly taken into account in the equations. Although the inverted remanent magnetization is including VRM—in contrast to ChRM determined in the laboratory—there might be a decay or gain of VRM between the measurements with the new approach and the laboratory measurements. Due to the rotation of the samples, there might also be a change in VRM during the approx. 1.5 h measurement with the new set-up, which is not explicitly taken into account within the equations.
3. The daub sample was carefully placed in the middle of the cardboard box. Nevertheless, we cannot exclude that the magnetic centre is deviating from the centre of the cardboard box und thus the point of rotational origin. This could also produce a small shift.
4. A constant term in the equations is given by the input of magnetic susceptibility. A comparison of results between susceptibilities measured with different methods shows that the susceptibilities measured with the surface sensor are clearly smaller than those measured in the laboratory. This is due to different reasons: The first is the difficult coupling of the surface sensor to the sample, because the sample surface was very rough and thus air gaps are included in the measured volume. Although several measurements were conducted on the surface of the samples, it was not possible to find a position with perfect coupling to the sample. Therefore, we conclude that the laboratory measurements where subsamples are measured inside the homogeneous field of a solenoid are the 'true' values of susceptibility. They have also proved that there is no difference between susceptibilities of inner and outer parts of the samples. The second reason could also be a possible difference in calibration of the instruments, although we assume this factor to be not as important as the first one, because both instruments were calibrated on reference samples before the measurements and also the drift was eliminated.

Regarding the first three reasons mentioned before, we do not have evidence for or against them. But at least we can do a test on the effect of the last reason: We need to investigate if the inversion results are sensitive to susceptibility variations. Therefore, we inverted again for the NRM vector using different susceptibilities in the range 100–3000e-5 SI as input. Figure 6a shows the observed and modelled curves for sample 10073, which are close together. The

TABLE 3 Surface magnetic susceptibilities for all five samples

Sample #	Mean (*1e-5 SI)	Median (*1e-5 SI)	Standard deviation (*1e-5 SI)	Median mass susceptibility (*1e-8 m^3/kg)
10067	529	545	99	374
10070	663	666	120	557
10071	781	740	223	491
10072	750	747	110	526
10073	741	716	167	438

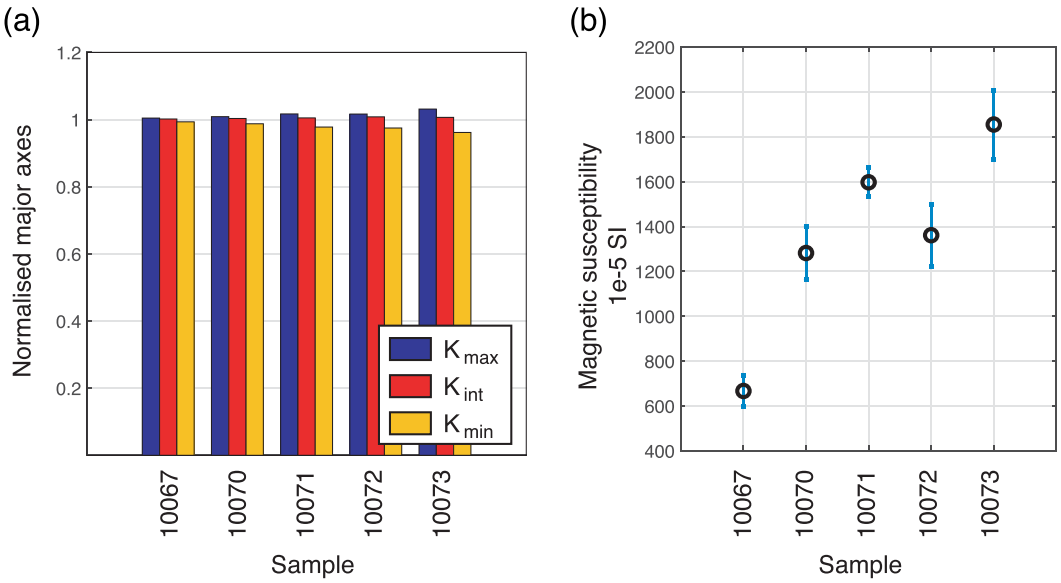

FIGURE 4 (a) Anisotropy of the magnetic susceptibility and (b) mean and standard deviation of magnetic susceptibility measured in laboratory [Colour figure can be viewed at wileyonlinelibrary.com]

susceptibility only produces a constant offset to the observed curve, which is getting smaller for increasing susceptibility. The resulting NRM for this susceptibility range does not vary much (only in the fourth decimal place), whereas the RMS error decreases slightly for increasing susceptibility due to smaller constant offsets (Figure 6b). The solution for the surface susceptibility measurement is somewhere in the middle and does not have the smallest RMS error. This is also true for all other samples (Figure 6c) and also if the higher laboratory susceptibility would be used as input. The percentage variations of the resulting NRM using the given susceptibility range are small for all samples: max. 0.8% for inclination, max. 4.5% for declination and 0.9% for intensity. These findings lead us to the conclusion that the inversion result is (almost) independent of chosen susceptibility, at least for a wide range and for the investigated samples.

Taking the laboratory susceptibilities as 'true' values, we think that the constant offset between observed and modelled curve has a different origin than incorrect susceptibility (i.e. reasons one to three). Because we cannot clearly name the origin of the offset, we simply assume an induced magnetization of 0 A/m (i.e. susceptibility = 0) and add the constant offset as inversion parameter in addition to the NRM vector. As mentioned before, test calculations have shown that the resulting NRM vector is not influenced by this offset. All subsequent inversion calculations are then performed with this fourth parameter (see Figure 7 for observed and modelled points for the other samples). For sample 10067, the resulting RMS error between observed and modelled points is then 0.26 nT (~6.2%) (Figure 5b), which is less compared with the inversion without constant offset (0.32 nT; Figure 5a). Figure 5c,d shows the fit between observed and modelled points for the reduced datasets for sample 10067. For 22 points, only approximately two wavelengths of the sinusoidal curve are used and for six measurement points only one wavelength. The fit is worse compared with the complete dataset (Figure 5b) with some outliers.

The results for inclination, declination, intensity and offset for all geometrical parameterizations and complete and reduced datasets are presented in Figure 8 (and listed in Table A2). Generally, the results for I_{rem}, D_{rem} and M_{rem} are very close to each other for the three geometrical parameterizations. Using reduced datasets of 22 or 6 measurement points show similar results for all three geometries, but differences to the complete dataset: deviations of max. 14.7° for the inclination, max. 15.1° for the declination, max. 0.36 A/m for the intensity and max. 0.12nT for the offset. The RMS errors for the reduced dataset are calculated using the NRM values and offset from the inversion with the reduced dataset to model the data for the

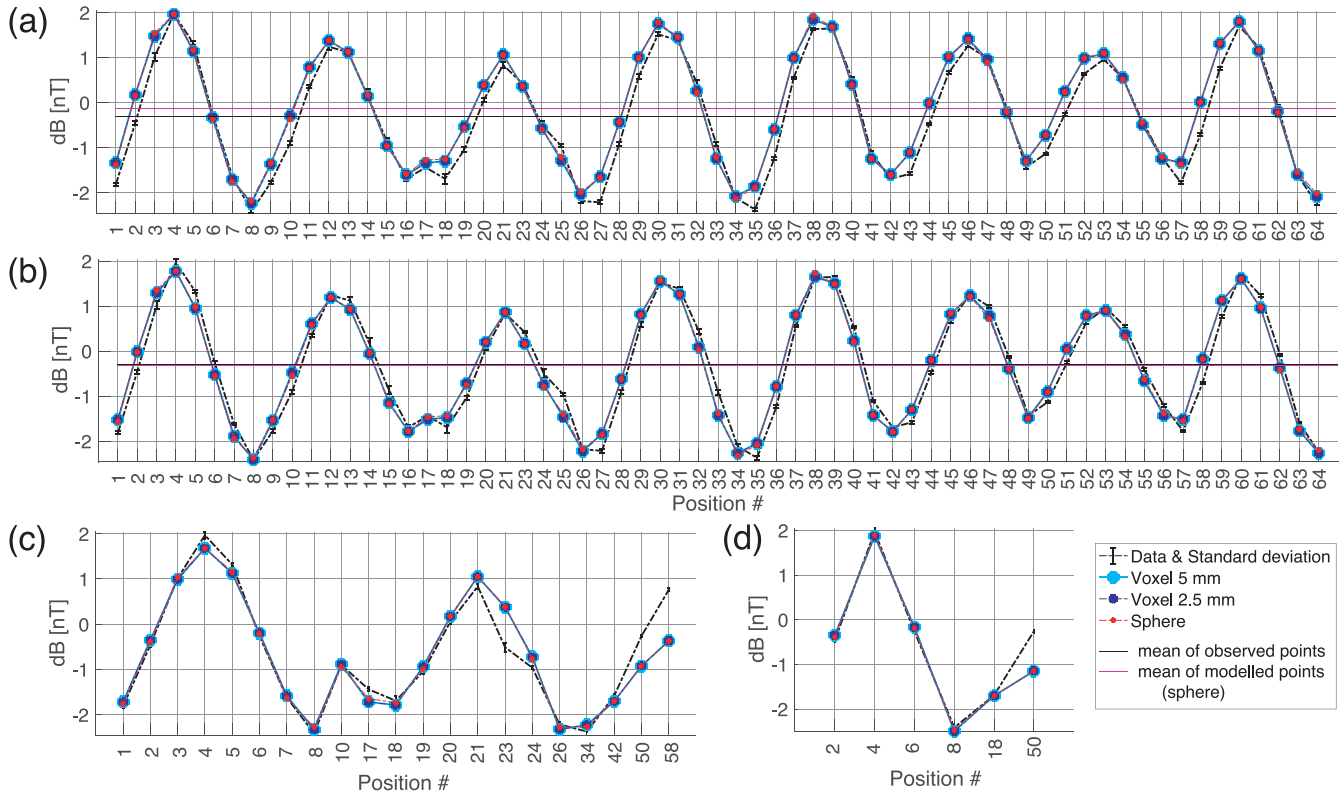

FIGURE 5 (a) Observed and modelled points for sample 10067 for all geometrical approximations; (b) observed and modelled points for sample 10067 for the inversion including a constant offset as inversion parameter. Observed and modelled points for the inversion including a constant offset for the reduced data sets: (c) 22 points and (d) 6 points. Note that the lines between points are for illustration purposes only [Colour figure can be viewed at wileyonlinelibrary.com]

complete dataset and then compares the observed and modelled points for the complete set. They increase strongly (more than 350% for sample 10070) if the dataset is reduced. Thus, a measurement time reduction is not feasible.

The NRM directions from the five samples show a wide range with mostly positive inclination (except of sample 10070 with negative inclination). The NRM intensities range between 0.9 and 3.2 A/m.

3.3 | Validation of underlying simplifying assumptions of the inversion

The results presented before have shown that the spherical representation of the sample gives approximately the same NRM values as the (exact) voxel model. To evaluate under which conditions the assumption of using a sphere as geometrical parameterization is valid, we modelled field values for different virtual samples with a wide range of parameters. For each of the combinations of parameters in Table 4, a box model and a sphere model with the same volume were compared. The induced magnetization was neglected for all calculations (as was done in the inversion computations above). The volume of each box model was calculated using the lengths of the sides, and an equivalent radius of a sphere was calculated. In addition, we calculated the dipole moment by multiplying the magnetization with the volume.

From the modelled curves for sphere and box, the RMS error between both curves was determined and the range of the values from the box model. For a successful measurement, the range of values has to be detectable, that is, the range has to be larger than the noise level (Condition 1). The assumption of using a sphere is valid under the condition that the RMS error between both modelled curves is smaller than the sensitivity of the magnetometer (Condition 2). In order to investigate for which parameters these two conditions are satisfied, the equivalent radius and the dipole moment were plotted against the distance between sensor and sample (Figure 9a,b, red points). Because for each of these parameter combinations the RMS error and the range were determined, we can mark those models that satisfy both conditions (Figure 9a,b, blue squares). Condition 1 determines the lower bound of radius or dipole moment and Condition 2 the upper bound. Below the bound of Condition 1, the range of measured values is too small to be detectable, and above the bound of Condition 2, the assumption of using a sphere parameterization is not valid. Although there are still some 'invalid' models inside the bounds, we try to estimate empirical functions that determine these bounds and thus can be used for generalization. For the radius versus distance, both conditions can be fitted by linear functions ($r = a \cdot x$,

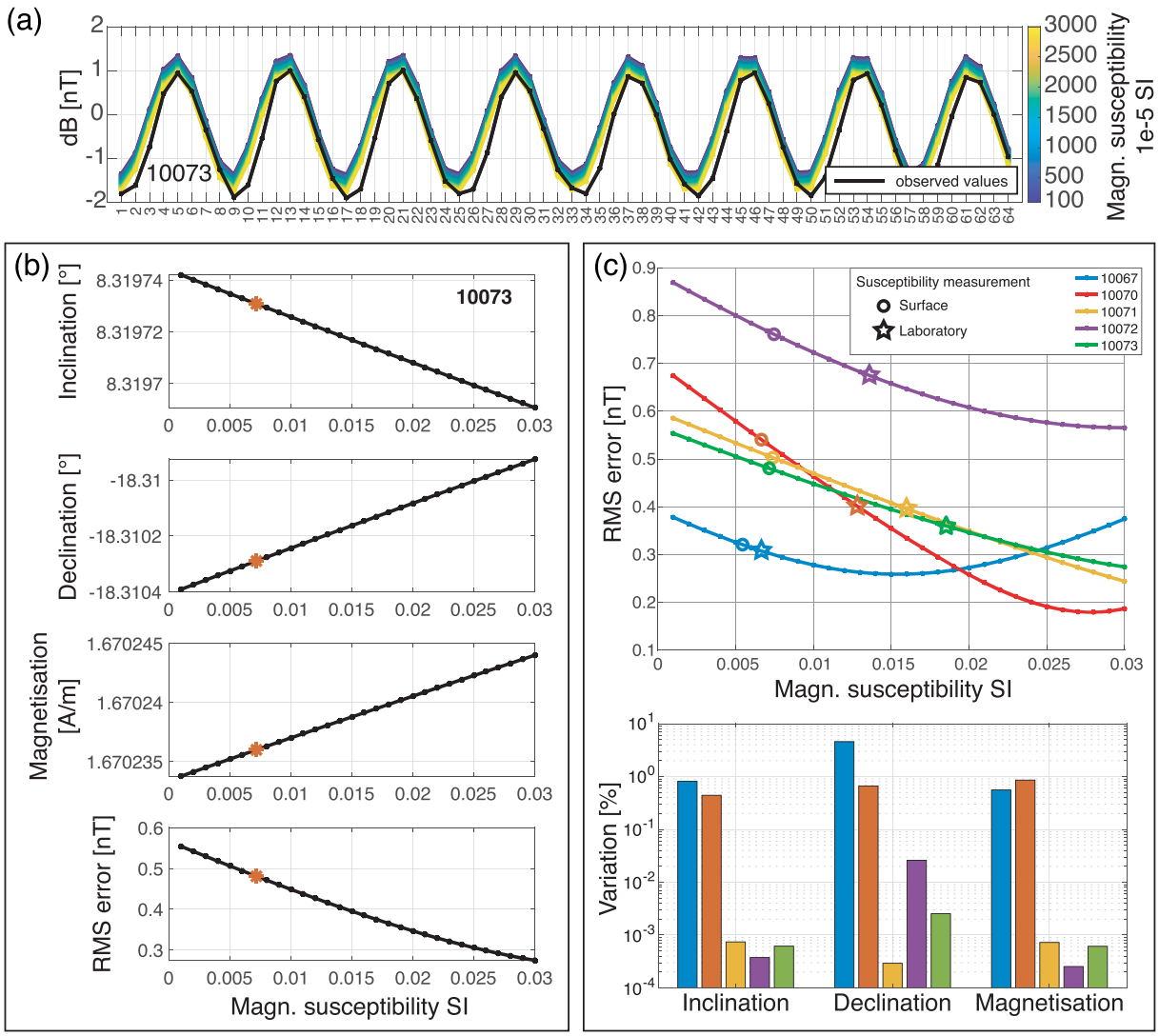

FIGURE 6 (a) Observed and modelled curves for different susceptibilities for sample 10073; (b) inversion results and RMS error for different susceptibilities for sample 10073; (c) RMS error versus susceptibility for all samples and percentage variations of the results in the reported susceptibility range for all samples [Colour figure can be viewed at wileyonlinelibrary.com]

with r being radius, x distance and a coefficient to be determined by fitting), whereas for the dipole moment versus distance, a function of the form $m = a \cdot x^3$ was used (m, dipole moment; x, distance; a, coefficient to be determined by fitting). For increasing noise level and increasing sensitivity, the lines of both conditions have increasing gradients (Figure 9c,d). In our measurements, we can assume a noise level, that is, a standard deviation of the measurement, of ±0.1 nT and the sensitivity of the caesium magnetometer is ±0.02 nT. Under these assumptions, all samples from this study are in the valid area were both conditions are satisfied (black points in Figure 9c,d). The results are not depending on NRM direction as all directions listed in Table 4 (I_{rem} and D_{rem}) produced the same findings. In our measurement set-up, the valid range of radii is between 7.9 mm and 7.9 cm, and the valid range of dipole moments between 1.7e-5 and 5.7e-3 A/m^2.

To determine the valid range for future measurements, one can use an empirical generalization to calculate the coefficients (gradients) of both the linear and cubic functions for different noise levels and sensitivities that are dictated by the magnetometer used. The empirical fitting functions for the determination of the coefficients were found by plotting the coefficients for different noise levels and sensitivities (Figure 10). They can be fitted by logarithmic and linear functions that are listed in Table 5.

3.4 | Validation through laboratory measurements

To check the correctness of our results, we compare the NRM directions and intensities determined with the new method to the laboratory measurements, which we define as 'true'. From the laboratory measurements, we used the NRM results and not ChRM, because in our approach measurements include the VRM, too. First, we present the results of the NRM determined in laboratory and then compare these values to the results from our new approach.

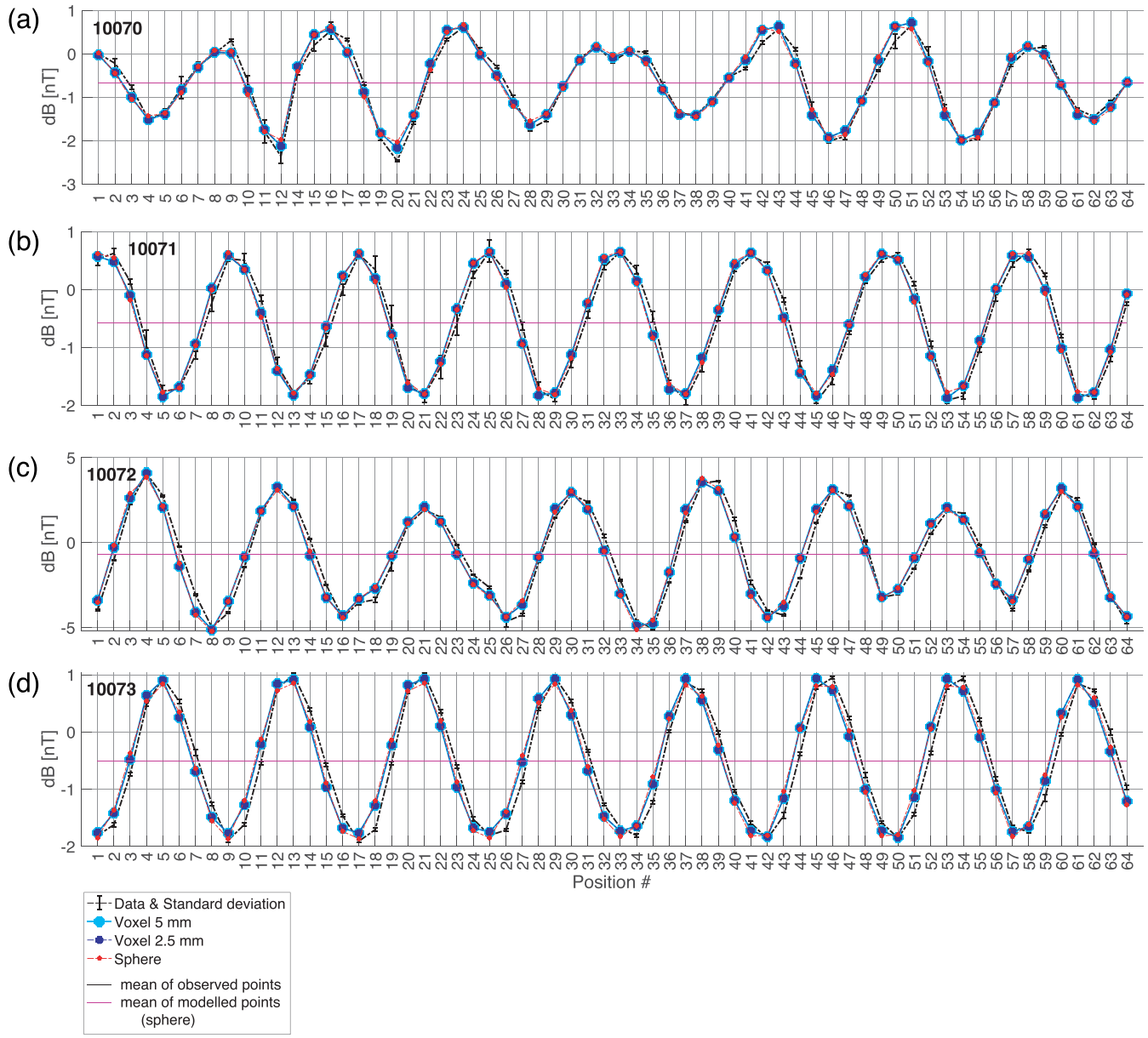

FIGURE 7 Observed and modelled points for samples (a) 10070, (b) 10071, (c) 10072 and (d) 10073, including a constant offset as inversion parameter. Note that the lines between points are for illustration purposes only [Colour figure can be viewed at wileyonlinelibrary.com]

3.4.1 | NRM and ChRM

Figure 11 shows the results from NRM and ChRM measured on the 6 cm^3 cubic subsamples in the laboratory. Sample 10072 has a higher magnetization of 3.73 A/m compared with the other samples with magnetizations between 1.31 and 1.73 A/m. Sample 10070 has a negative inclination of −18° and the largest error with a 95% confidence ellipse of 11.7°. All other samples have positive inclination and smaller errors. The declinations are widely distributed between −18° and 160°. The ChRM values, which do not contain VRM contributions anymore, show smaller ranges and smaller errors compared with NRM directions (Figure 11). The maximum difference in inclination is 17.4° and in declination 3.4° between mean NRM and ChRM. The difference between NRM and ChRM reveals the presence of VRM, which was not accounted for in our approach. Therefore, we compare the results from our approach to the laboratory NRM values, which still include VRM.

3.4.2 | Comparison of our approach with validation measurements

In Figure 12, the results (inclination, declination and intensity of NRM) of the new approach are compared with the 'true' values of NRM resulting from the laboratory measurements. The results of the new approach show high similarity between the results for all

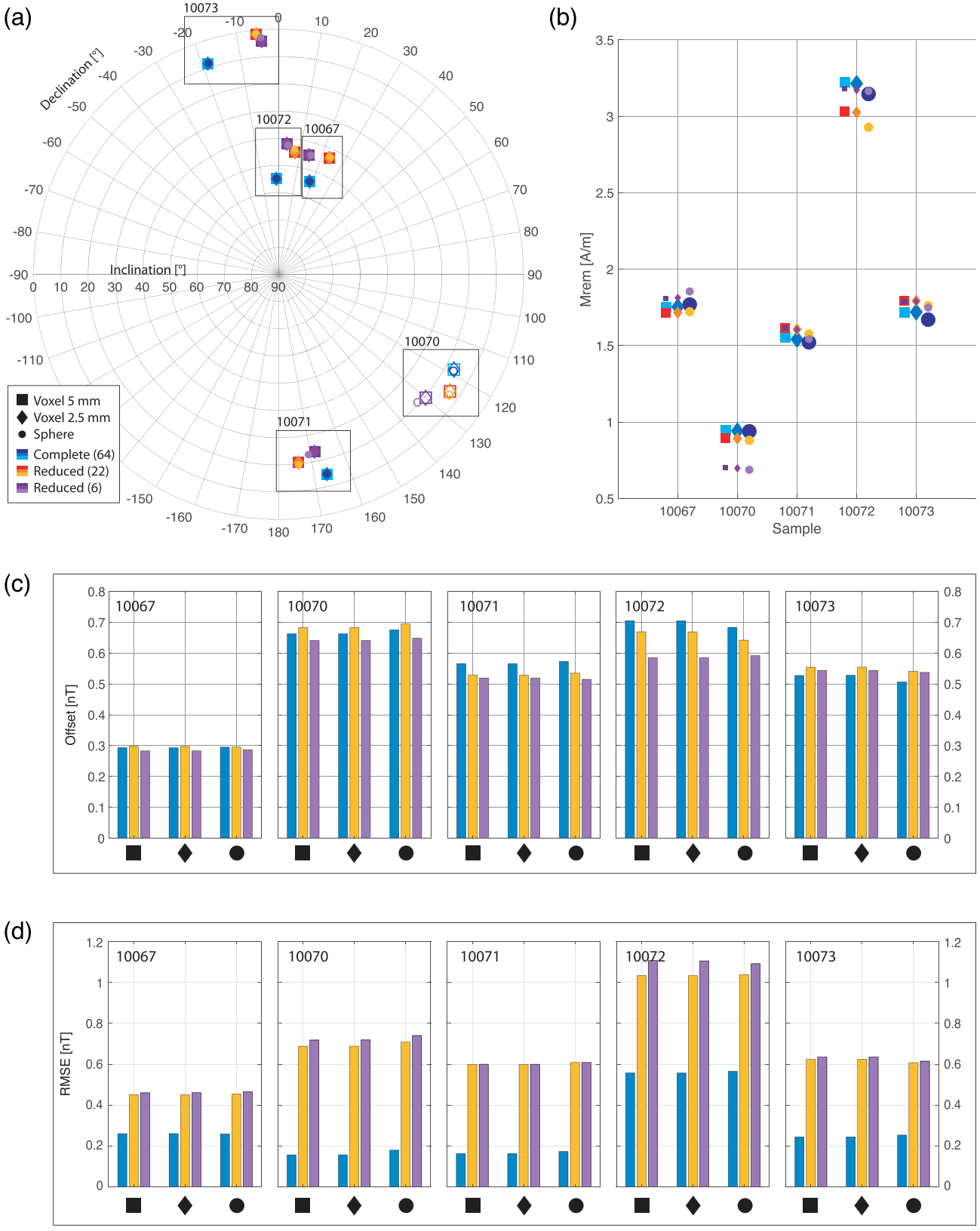

FIGURE 8 (a) Direction of inverted NRM for all samples and all inversion approaches. Note that open symbols indicate negative inclination (sample 10070). (b) Intensity of the NRM for all samples and inversion approaches, (c) determined offset and (d) RMS error between observed and modelled data [Colour figure can be viewed at wileyonlinelibrary.com]

TABLE 4 List of all parameters used for the modelling study

Parameter	Values	Comment
I_{rem} (°)	52.5, −21.5, 14.6, 53.6, 10.0	Same as for samples in this study
D_{rem} (°)	31.4, 120.1, 159.1, 18.6, −18.2	
M_{rem} (A/m)	0.1, 0.5, 1, 1.5, 2, 2.5, 3, 3.5, 4, 4.5, 5, 5.5, 6, 6.5, 7, 7.5, 8, 8.5, 9, 9.5, 10	
Distance sensor–sample (m)	0.1, 0.2, 0.3, 0.4, 0.5, 0.6, 0.7, 0.8, 0.9, 1, 1.5, 2, 3	Condition: has to be larger than half of max. length of sample
Length of box in x (m)	0.01, 0.05, 0.1, 0.2, 0.3, 0.4	Limited by practical reasons considering the gimbal and rotation
Length of box in y (m)	0.01, 0.05, 0.1, 0.2, 0.3, 0.4	
Length of box in z (m)	0.01, 0.05, 0.1, 0.2, 0.3, 0.4	
Measurement positions	64	Distributed according to the virtual measurement positions used in this study

discretization approaches, but the deviation to the validation measurements increases for decreasing number of measurement positions (Figure 12). For 64 measurement positions, the results are in the error range of the validation measurements, except for sample 10072 and the declination of samples 10067 and 10071. The maximum errors in inclination and declination are 1.7° and 20°, respectively, and in intensity 0.6 A/m, which is about 28% (sample 10070), but still in the error range of the validation measurements.

For reduced datasets of 22 or 6 positions, the results are mostly out of the error range of the validation measurements. Thus, a reduced dataset is not feasible, at least for most of the samples. In general, the inclination and also the magnetization intensity are reproduced well with our approach compared with the validation measurements, whereas the determination of the declination shows deviations from the validation measurements of up to 20° in the worst case (sample 10072). In conclusion, we can state that our newly proposed approach using 64 measurements produces acceptable results mostly in the error range of laboratory measurements and that the assumption of using a spherical model is sufficient.

4 | DISCUSSION

4.1 | Comparison with other studies

A number of approaches for determining the remanent magnetization without laboratory instruments have been published previously. Clark (2014) provides an overview of some of them, inter alia, constrained modelling with given geometry or depth (Hall, 1959), direct inversion using magnetic sources with simple given geometry, and combining magnetic and gravity data (Garland, 1951). These methods aim at determining the magnetization of particular buried objects from measurement of the magnetic field at the earth surface. The outcome is bulk magnetization of the object as a whole, for example, a pit house, a ditch or the burnt remains of Neolithic Tripolye houses (e.g. Rassmann et al., 2014), which motivated the present study (Pickartz et al., 2019). In a general sense, our approach can be regarded in this context as a special case of the methods revisited by Clark (2014) of direct constrained inversion regarding the shape and susceptibility of the source. However, the original aim of our approach is to enable validation of inversions results of field measurements through on-site measurements of samples taken of these larger buried objects. Of course, it can also be applied to characterize archaeological finds independently of actual magnetic surveying.

Other such archaeological samples that could be investigated with our method are, for example, bricks from ancient walls, tiles and pottery (shards). Chlupáčová et al. (2012) have shown that pottery from southern Bohemia from the La Tène period and the Middle Ages have high NRM intensities of up to 44 A/m. According to various rock magnetic analyses, this is due to maghemite and subordinate magnetite and hematite, which were not seen with an optical microscope. Thus, analyses of the NRM helped in the determination of mineral composition and also in the determination of the firing conditions (reduction or oxidation). The advantage of using our proposed method would be that the pottery would not have been destroyed. This is especially advantageous if the pottery shards need to be fit together, as was done in a study of Burnham and Tarling (1975). They tested the Digico complete results magnetometer (Molyneux, 1971) if it could be also used with samples of arbitrary shape by placing the shards in a Perspex box and rotating them on a platform. After complete rotation around the vertical axis, the Perspex box with the sample had to be turned around, and the rotation of the platform had to be repeated. They could successfully determine the NRM of the shards and thus use them to fit the shards together (Burnham & Tarling, 1975). Ntoukakis et al. (2019) used a similar approach with shards placed on a rotating platform and measurements with three-axis fluxgate magnetometers. An additional help for the fitting of the vases is the potter's mark or the decoration on the shards. Our approach can also be used to measure the NRM of shards, and in contrast to the method of Burnham and Tarling (1975), who had to turn the Perspex box with the shard manually on the rotating platform to achieve different orientations of the sample, we rotate the sample box in the same place and thus can avoid errors due to misplacement.

The determination of NRM of shards can be used for the reconstruction of, for example, vases, but it can also be used to date the archaeological artefacts under certain conditions: The vases acquired their TRM during firing and cooling and if they are destroyed later and fitted together today only the determined inclination can be used for archaeomagnetic dating under the assumption that they were burnt and cooled upright. The declination cannot be used, because the

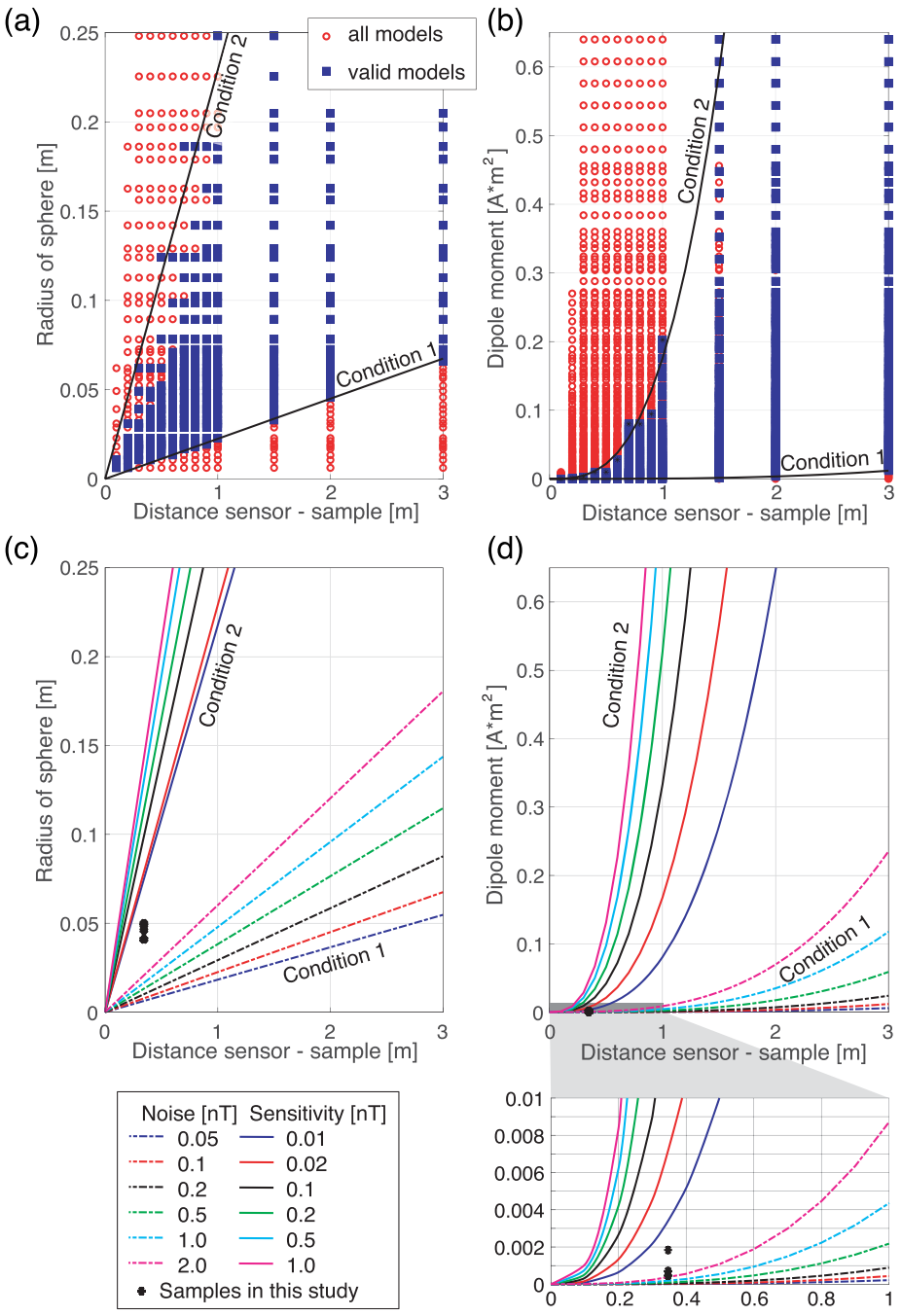

FIGURE 9 (a) Radius versus distance and (b) dipole moment versus distance for all parameter combinations in Table 4. The black lines mark the bounds of the valid area given by Condition 1 (range > noise level) and Condition 2 (RMSE < sensitivity). (c,d) The lines for the conditions for various noise levels and sensitivities as well as the samples in this study [Colour figure can be viewed at wileyonlinelibrary.com]

rotation of the vase towards north inside the kiln in ancient times cannot be reconstructed (Lanos et al., 1999).

4.2 | Archaeological implications of our results

The daub pieces used in our study originate from a burnt house built from loam and wood. Other studies, that is, Shaffer (1993) about a Neolithic settlement in Calabria, Italy, and Guerrero et al. (2015) about a Teuchitlán site in Mexico, have shown that daub pieces are carriers of remanent magnetization that can be used for firing–cooling–collapsing order determinations and archaeomagnetic dating. The NRM intensity of the daub pieces depends, among others, on the mineralogy of the clay used and on the intensity and duration of the burning (Shaffer, 1993). If the daub samples show NRM of different orientations, as in our study or in Shaffer (1993), the archaeological interpretation is that the building was standing upright while firing and cooling and thus acquiring a TRM and then collapsed. It cannot be deduced from the measurements whether this order is due to a delayed collapse of the building or some part of it only at the end of the cooling phase or whether the fire was applied long before the collapse for constructive reasons. Gradual collapse of house walls over a period of several hours was for example observed in the case of an experimentally burnt house in the Tripolye settlement of Nebelivko

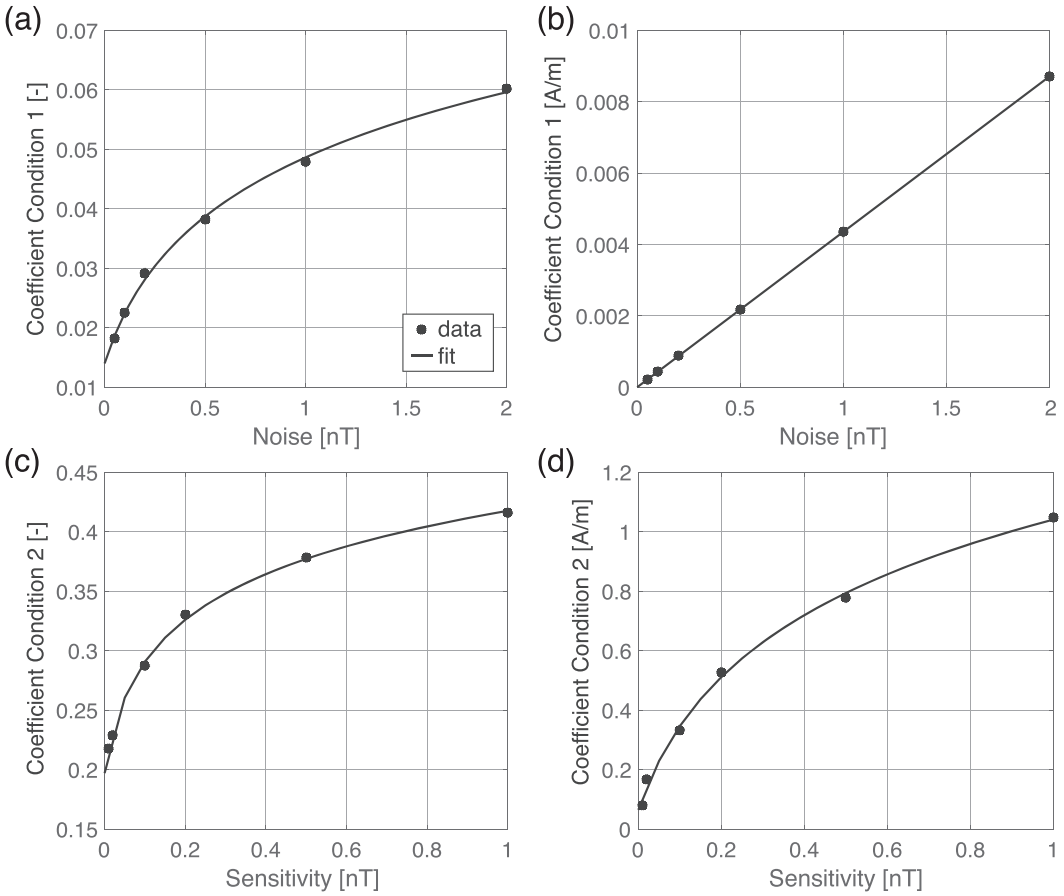

FIGURE 10 Coefficients for Condition 1 ((a) radius versus distance, (b) dipole moment versus distance) and Condition 2 ((c) radius versus distance, (d) dipole moment versus distance) for various noise levels and sensitivities (dots) and empirically fitted functions listed in Table 5

TABLE 5 List of empirically determined fitting functions for the coefficients (a) depending on arbitrary noise level (n) and sensitivity (s)

Relationship	Condition	Figure	Fitting function
Distance–radius	1	Figure 9a	a = 0.018*log(13.43*n + 2.21)
Distance–dipole moment	1	Figure 9b	a = 0.004*n
Distance–radius	2	Figure 9c	a = 0.06*log(949.54*s + 25.73)
Distance–dipole moment	2	Figure 9d	a = 0.41*log(11.65*s + 1.17)

(Johnston et al., 2019). Post-depositional displacement processes, for example, due to weathering, should also be considered as factors for the deviations. For archaeomagnetic dating of wattle and daub buildings, the NRM intensity is used, which is determined through the Thellier-type double heating method (Guerrero et al., 2015; Thellier & Thellier, 1959). NRM directions are not useful except if the daub walls are still standing in situ and thus remain in their original orientation.

4.3 | Strengths and weaknesses of our approach

The weakness of our approach is that we can only determine NRM, but neither the ChRM direction nor the origin of the NRM, for example, TRM or DRM. If a VRM is present in the samples, it falsifies the determined NRM direction and intensity. In laboratory measurements, this is handled by stepwise demagnetization and thus removal of the VRM. In our approach, one possible solution to overcome the problem of VRM would be to place the sample for some time (several days) before the measurement in an orientation that can easily be turned for 180°. After this time, the possibly present VRM in the sample has mainly oriented itself in the direction of the present ambient magnetic field. If then the sample is turned around for 180°, the VRM will be acquired in opposite direction, and thus cancelling out. This is a method invented by Thellier and Thellier (1959) and further described in Perroud et al. (1991). The subsequent measurement of NRM should now be mainly independent of VRM. Of course, this procedure is not as accurate as demagnetization in the laboratory measurements, because the logarithmic time decay and acquisition of VRM are different for different materials and the rotation of the samples during the measurements might also have an effect on VRM. Additionally, our

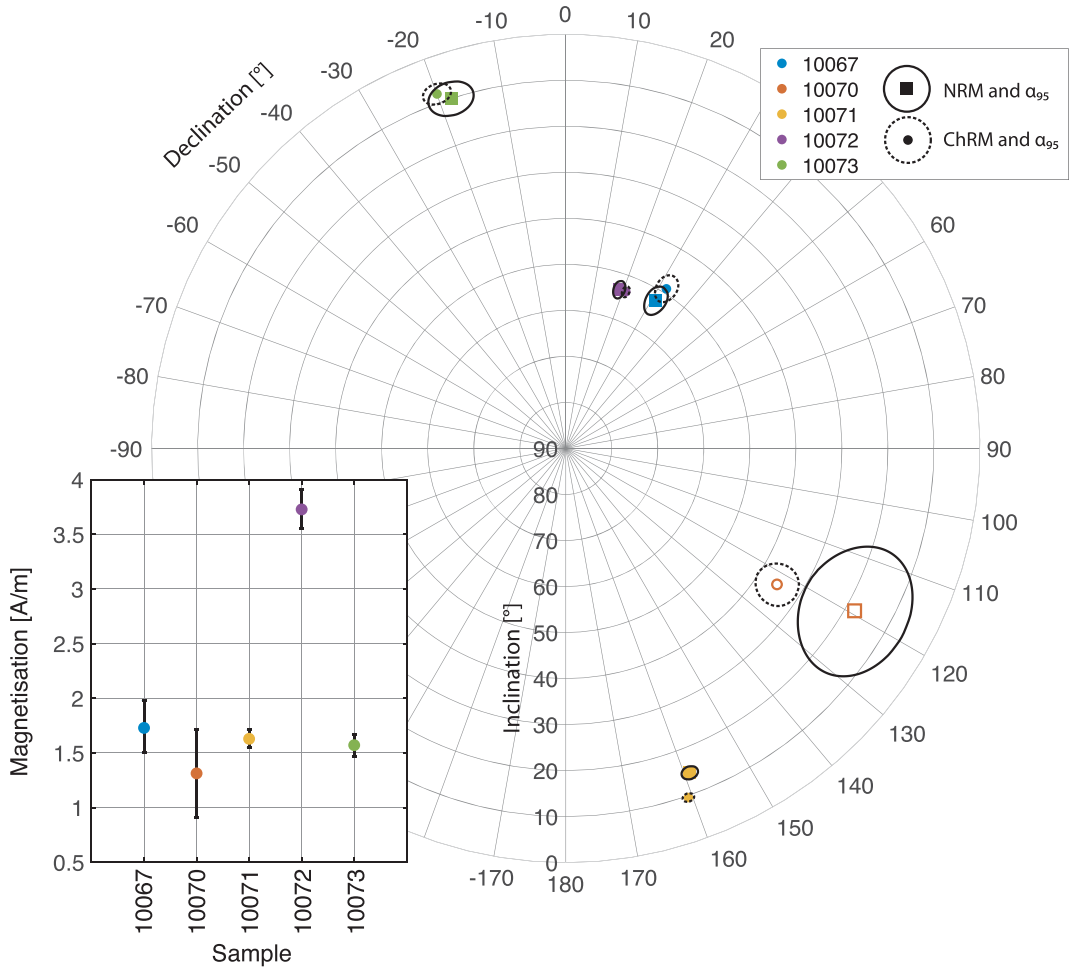

FIGURE 11 Results of the validation laboratory measurements of the NRM and ChRM for all samples with 95% confidence interval (α_{95}). Filled symbols indicate positive inclination, and open symbols negative inclination [Colour figure can be viewed at wileyonlinelibrary.com]

approach is not able to investigate the type of NRM carrying minerals, which provide the archaeomagnetic information.

The strengths of our proposed approach are clearly the non-destructive handling of the samples and the applicability to samples of arbitrary shape, and, to a certain degree, arbitrary size under consideration of a proper sensor distance, as was shown before. In addition, no extra laboratory instruments are necessary, and the measurement set-up can be taken to the field for sample measurements on-site, for example, if they cannot be exported from foreign countries.

5 | CONCLUSION

We developed a measurement set-up and numerical inversion scheme for the determination of the NRM vector of archaeological samples of arbitrary shape, which (1) is non-destructive, (2) is portable so it can be used for on-site measurements and (3) results in NRM direction and intensities comparable with laboratory-based analyses on standardized sample shapes, with the need to destroy the archaeological artefact. If a sensitive enough field magnetometer is already available, the proposed experimental set-up can also be regarded as a low-cost solution. Our test measurements, numerical computations and validation through highly accurate, independent laboratory measurements have shown that the proposed approach is capable of determining the NRM mostly inside the error range of the validation measurements. The inclination and declination of the NRM can be determined with accuracies better than 2° and 20°, respectively. The NRM intensity could be recovered with accuracy better than 0.6 A/m, which corresponds to 28%, but is still in the error range of the validation measurements. This is accurate enough for the firing–cooling–collapsing order determinations of wattle and daub buildings, the joining of shards to a vase and the use for magnetic modelling studies, which need the inclusion of the NRM vector of the source bodies. The use for palaeomagnetic dating has to be further investigated and, at least, is not feasible for our daub samples due to the reorientation during collapse of the building. For future measurements using this or a similar set-up, we recommend the following procedure:

1. Determine the volume of your archaeological sample, for example, through replacement of water by the sample, photogrammetric modelling or 3D scanning.

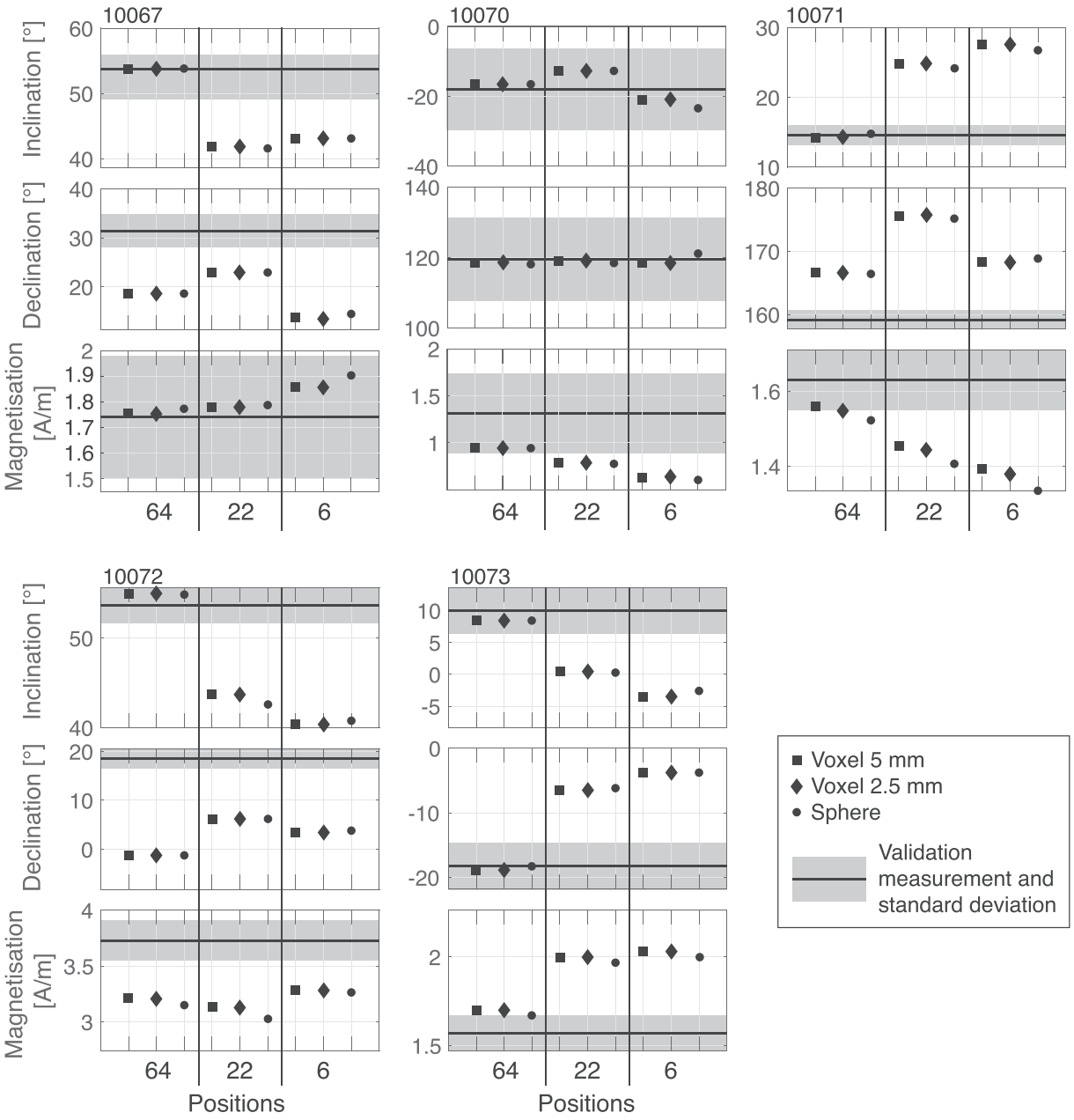

FIGURE 12 Comparison of results (I_{rem}, D_{rem} and M_{rem}) for all datasets (complete and reduced) and all geometrical representations with validation measurements (NRM)

2. Evaluate the conditions given in the text regarding expected noise level and magnetometer sensitivity in order to choose the minimum sensor-sample distance and adjust the measurement set-up if necessary. The magnetization has to be estimated in this step, because at this time it is not known yet. If the conditions are satisfied, the exact shape of the sample is not important and can be replaced by a sphere with the same volume.
3. Conduct the measurements using all 64 rotational positions. Calculate the mean values for each step.
4. Use the measurements to invert for the NRM vector and a constant offset, which accounts for various effects that cannot be controlled, such as small changes in the measurement setup, displacement of the magnetic centre and the effect of VRM.

ACKNOWLEDGEMENTS

The work was funded by the Deutsche Forschungsgemeinschaft (DFG, German Research Foundation) – Project-ID 290391021 – SFB 1266. We would like to thank A.S. Jagiolla, V. Hilberg, R. Erichsen and M. Bahns for their help and support during the measurements. Also thanks to the Open Source Projects CloudCompare (http://www.cloudcompare.org/) and MeshLab (https://www.meshlab.net/).

We would also like to thank two anonymous reviewers for their valuable comments that helped to improve the manuscript.

The samples analysed in this study were obtained within the framework of a cooperation between the Museum of Vojvodina Novi Sad and the Institute of Prehistory and Protohistory of the Christian-

Albrechts-University in Kiel. The excavations in Makaranda took place in August 2018 and was financed by funds of the Museum of Vojvodina, the project 'Interaction in the central and western Balkans during the Neolithic and Early Eneolithic' of the German Research Foundation (DFG project number Ho 5176/1). We thank our colleagues Aleksandar Medović, Tijana Stanković Pešterac, Ildiko Medović (Novi Sad) and Martin Furholt (Kiel) for the constructive cooperation and the uncomplicated provision of the samples.

CONFLICT OF INTEREST

The authors declare that they have no known competing financial interests or personal relationships that could have appeared to influence the work reported in this article. No conflict of interest has been declared by the authors.

AUTHOR CONTRIBUTIONS

T.W.: Writing–original draft, formal analysis, data curation, software, visualization. R.K.: Methodology, investigation, data curation, software. N.N.: Validation, investigation. N.P.: Writing–original draft, conceptualization. D.S.-K.: Investigation. R.H.: Resources. W.R.: Conceptualization, methodology, supervision, funding acquisition. All authors: Writing–review and editing.

DATA AVAILABILITY STATEMENT

The data that support the findings of this study are available from the corresponding author upon reasonable request.

ORCID

Tina Wunderlich https://orcid.org/0000-0003-2275-704X
Norbert R. Nowaczyk https://orcid.org/0000-0002-3362-0578
Natalie Pickartz https://orcid.org/0000-0002-3290-7032
Wolfgang Rabbel https://orcid.org/0000-0003-4720-6906

REFERENCES

Bartington. (n.d.). MS2 magnetic susceptibility system operation manual OM0408. https://www.bartington.com/wp-content/uploads/pdfs/operation_manuals/MS2_OM0408.pdf

Becker, H. (1995). From nanotesla to picotesla — A new window for magnetic prospecting in archaeology. *Archaeological Prospection*, *2*, 217–228. https://doi.org/10.1002/1099-0763(199512)2:4<217::AID-ARP6140020405>3.0.CO;2-U

Bhattacharyya, B. K. (1964). Magnetic anomalies due to prism-shaped bodies with arbitrary polarization. *Geophysics*, *29*(4), 517–531. https://doi.org/10.1190/1.1439386

Bis, W., Herbich, T., Ryndziewicz, R., Osiadacz, M., Radomski, M., Cembrzyński, P., Zbieranowski, M., & Majewski, J. (2021). An integrated geophysical and archaeological approach to the study of the late medieval castle in Żelechów in Mazovia, Poland. *Archaeological Prospection*, 1–19. https://doi.org/10.1002/arp.1820

Blakely, R. (1996). *Potential theory in gravity and magnetic applications*. Cambridge University Press.

Brami, M. N. (2017). *The diffusion of neolithic practices from Anatolia to Europe. A contextual study of residential construction, 8,500–5,500 BC cal*. BAR International Series 2838. BAR Publishing.

Burnham, R., & Tarling, D. (1975). Magnetization of shards as an assistance to the reconstruction of pottery vessels. *Studies in Conservation*, *20*(3), 152–157. https://doi.org/10.2307/1505680

Chlupáčová, M., Hrouda, F., Niìoanský, D., Procházka, V., Petáková, Z., & Laufek, F. (2012). Frequency-dependent susceptibility and other magnetic properties of Celtic and mediaeval graphitic pottery from Bohemia: An introductory study. *Studia Geophysica et Geodaetica*, *56*, 803–825. https://doi.org/10.1007/s11200-011-9011-y

Cignoni, P., Callieri, M., Corsini, M., Dellepiane, M., Ganovelli, F., & Ranzuglia, G. (2008). MeshLab: An open-source mesh processing tool. *Computing*, *1*, 129–136.

Clark, D. A. (2014). Methods for determining remanent and total magnetisations of magnetic sources – A review. *Exploration Geophysics*, *45*, 271–304. https://doi.org/10.1071/EG14013

Fisher, R. (1953). Dispersion on a sphere. *Proceedings of the Royal Society of London a*, *217*, 295–305. https://doi.org/10.1098/rspa.1953.0064

Gapeev, A. K., Gribov, S. K., Dunlop, D. J., Özdemir, Ö., & Shcherbakov, V. P. (1991). A direct comparison of the properties of CRM and VRM in the low-temperature oxidation of magnetite. *Geophysical Journal International*, *105*(2), 407–418. https://doi.org/10.1111/j.1365-246X.1991.tb06722.x

Garland, G. D. (1951). Combined analysis of gravity and magnetic anomalies. *Geophysics*, *16*, 51–62. https://doi.org/10.1190/1.1437650

Geometrics. (2004). G-822A and G-823A and B cesium magnetometer operation manual. Geometrics Inc., 190 Fortune Drive, San Jose, CA 95131 USA.

Guerrero, A. T., Goguitchaichvili, A., Lopez, R. E., Molares, J., Elguera, J. R., Soler, A. M., Cardenas, E., & Urrutia-Fucugauchi, J. (2015). A detailed rock-magnetic and archaeomagnetic investigation on wattle and daub building (Bajareque) remains from Teuchitlan tradition (nw Mesoamerica). *Journal of Archaeological Sciences: Reports*, *5*, 564–573.

Hall, D. H. (1959). Direction of polarization determined from magnetic anomalies. *Journal of Geophysical Research*, *64*, 1945–1959. https://doi.org/10.1029/JZ064i011p01945

Herries, A. I. R. (2009). New approaches for integrating palaeomagnetic and mineral magnetic methods to answer archaeological and geological questions on stone age sites. In A. S. Fairbairn, S. O'Connor, & B. Marwick (Eds.), *New directions in archaeological science* (pp. 235–253). The Australian National University Press.

Hofmann, R., Medović, A., Furholt, M., Medović, I., Stanković-Pešterac, T., Dreibrodt, S., Martini, S., & Hofmann, A. (2019). Late neolithic multicomponent sites of the Tisza region and the emergence of centripetal settlement layouts. *Prähistorische Zeitschrift*, *94*(1), 1–28.

Johnston, S., Chapman, J., Gaydarska, B., Diachenko, A., Voke, P., Nebbia, M., & Litkevych, V. (2019). The Nebelivka experimental house construction and house burning, 2014-2015. *Bulgarian e-Journal of Archaeology*, *9*(1), 61–90.

Jordanova, N., Jordanova, D., Kostadinova-Avramova, M., Lesigyarski, D., Nikolov, V., Katsarov, G., & Bacvarov, K. (2018). A mineral magnetic approach to determine paleo-firing temperatures in the neolithic settlement site of Mursalevo-Deveboaz (SW Bulgaria). *Journal of Geophysical Research: Solid Earth*, *123*, 2522–2538. https://doi.org/10.1002/2017JB015190

Kirschvink, J. L. (1980). The least-squares line and plane and the analysis of palaeomagnetic data. *Geophysical Journal International*, *62*(3), 699–718. https://doi.org/10.1111/j.1365-246X.1980.tb02601.x

Lanos, P., Kovacheva, M., & Chauvin, A. (1999). Archaeomagnetism, methodology and applications: Implementation and practice of the Archaeomagnetic method in France and Bulgaria. *European Journal of Archaeology*, *2*(3), 365–392. https://doi.org/10.1179/eja.1999.2.3.365

Linford, N., Linford, P., Martin, L., & Payne, A. (2007). Recent results from the English Heritage caesium magnetometer system in comparison with recent fluxgate gradiometers. *Archaeological Prospection*, *14*, 151–166. https://doi.org/10.1002/arp.313

Medović, A., Hofmann, R., Stanković-Pešterac, T., Dreibrodt, S., Medović, I., & Pešterac, R. (2014). The late neolithic settlement mound

Bordoš near Novi Bečej, Serbian Banat, in a multiregional context - preliminary results of geophysical, geoarchaeological and archaeological research. *Rad Muzeja Vojvodina*, *56*, 53–77.

Miller, B. K., Furholt, M., Bayarsaikhan, J., Tüvshinjargal, T., Brandtstätter, L., Wright, J., Ayush, T., & Wunderlich, T. (2019). Proto-urban establishments in inner Asia: Surveys of an iron age walled site in eastern Mongolia. *Journal of Field Archaeology*, *44*(4), 267–286. https://doi.org/10.1080/00934690.2019.1598170

Molyneux, L. (1971). A complete result magnetometer for measuring the remanent magnetisation of rocks. *Geophysical Journal of the Royal Astronomical Society*, *24*, 429–433. https://doi.org/10.1111/j.1365-246X.1971.tb02188.x

NOAA. (2021). Magnetic field calculator. https://www.ngdc.noaa.gov/geomag/calculators/magcalc.shtml#igrfwmm (accessed 16 June 2021)

Ntoukakis, M., Pantinakis, A., Vafidis, A., & Markopoulos, T. (2019). Selection of co-belonging ceramic fragments from archaeological excavations and their location in vase bodies from Thermoremanent magnetization. *Applied Sciences*, *9*(16), 3310. https://doi.org/10.3390/app9163310

Perroud, H., Calza, F., & Khattach, D. (1991). Paleomagnetism of the Silurian volcanism at Almaden, southern Spain. *Journal of Geophysical Research*, *96*(B2), 1949–1962. https://doi.org/10.1029/90JB02226

Pickartz, N., Hofmann, R., Dreibrodt, S., Rassmann, K., Shatilo, L., Ohlrau, R., Wilken, D., & Rabbel, W. (2019). Deciphering archaeological contexts from the magnetic map: Determi-nation of daub distribution and masses of chalcolithic house remains. *The Holocene*, *29*(10), 1637–1652. https://doi.org/10.1177/0959683619857238

Rassmann, K., Ohlrau, R., Hofmann, R., Mischka, C., Burdo, N., Videjko, M. Y., & Müller, J. (2014). High precision Tripolye settlement plans, demographic estimations and settlement organization. *Journal of Neolithic Archaeology*, *16*, 96–134. https://doi.org/10.12766/jna.2014.3

Shaffer, G. D. (1993). An archaeomagnetic study of a wattle and daub building collapse. *Journal of Field Archaeology*, *20*(1), 59–75.

Thellier, E., & Thellier, O. (1959). Sur l'intensité du champ magnétique terrestre dans le passé historique et géologique. *Annales de Geophysique*, *15*, 285–376.

Wilken, D., Wunderlich, T., Stümpel, H., Rabbel, W., Pašteka, R., Erkul, E., Papčo, J., Putiška, R., Krajňák, M., & Kušnirák, D. (2015). Case history: Integrated geophysical survey at Katarínka monastery (Slovakia). *Near Surf. Geophys.*, *13*, 585–599. https://doi.org/10.3997/1873-0604.2015027

How to cite this article: Wunderlich, T., Kahn, R., Nowaczyk, N. R., Pickartz, N., Schulte-Kortnack, D., Hofmann, R., & Rabbel, W. (2022). On-site non-destructive determination of the remanent magnetization of archaeological finds using field magnetometers. *Archaeological Prospection*, *29*(2), 205–227. https://doi.org/10.1002/arp.1847

APPENDIX A

A.1 | Set-up of the inversion problem using a voxel model

The anomalous magnetic field of a cube (or voxel) with induced and remanent magnetization can be determined using following formula (Bhattacharyya, 1964):

$$\begin{aligned}\Delta B = C_m M \Bigg[& \frac{\alpha_{23}}{2} log\left(\frac{r-x'}{r+x'}\right) + \frac{\alpha_{13}}{2} log\left(\frac{r-y'}{r+y'}\right) \\ & - \alpha_{12} log(r+z_1) - \hat{M}_x f_x arctan\left(\frac{x'y'}{xr^2 + rz_1 + z_1^2}\right) \\ & - \hat{M}_y f_y arctan\left(\frac{x'y'}{r^2 + rz_1 - xr^2}\right) \\ & + \hat{M}_z f_z arctan\left(\frac{x'y'}{rz_1}\right) \Bigg] \Bigg|_{x'=x_1}^{x'=x_2} \Bigg|_{y'=y_1}^{y'=y_2}\end{aligned} \tag{1}$$

with $\alpha_{12} = \widehat{M_x} f_y + \widehat{M_y} f_x$, $\alpha_{13} = \widehat{M_x} f_z + \widehat{M_z} f_x$, $\alpha_{23} = \widehat{M_y} f_z + \widehat{M_z} f_y$, $r^2 = xr^2 + yr^2 + z_1^2$.

r is the distance from the magnetometer to the cube if the magnetometer is located at x = 0, y = 0 and z = 0 m. $C_m = 10^{-7}$ H/m is a constant, $\vec{M} = M \cdot \left(\widehat{M_x}; \widehat{M_y}; \widehat{M_z}\right) = (M_x; M_y; M_z)$ is the magnetization and the unit vector $(f_x; f_y; f_z) = (cos(I) \cdot cos(D); cos(I) \cdot sin(D); sin(I))$ is the direction of the normalized regional magnetic field defined by inclination I and declination D.

Equation 1 describes a prism with top at z_1 and bottom at infinity. Therefore, it has to be evaluated twice in order to subtract a cube with top at z_2 and bottom at infinity to result in a cube with top at z_1 and bottom at z_2. If the equations for α_{12},α_{13} and α_{23} are used, Equation 1 can be remodelled to show that it is linearly depending on the three components of the magnetization:

$$\begin{aligned}\Delta B = & M_x \cdot C_m \left(\frac{f_z}{2} \cdot L_2 - f_y \cdot L_3 - f_x \cdot A_1\right) + M_y \cdot C_m \left(\frac{f_z}{2} \cdot L_1 - f_x \cdot L_3 - f_y \cdot A_2\right) \\ & + M_z \cdot C_m \left(\frac{f_y}{2} \cdot L_1 + \frac{f_x}{2} \cdot L_2 + f_z \cdot A_3\right) \Bigg|_{x'=x_1}^{x'=x_2} \Bigg|_{y'=y_1}^{y'=y_2}\end{aligned} \tag{2}$$

with $A_1 = arctan\left(\frac{x'y'}{xr^2 + rz_1 + z_1^2}\right)$, $A_2 = arctan\left(\frac{x'y'}{r^2 + rz_1 - xr^2}\right)$, $A_3 = arctan\left(\frac{x'y'}{rz_1}\right)$, $L_1 = log\left(\frac{r-x'}{r+x'}\right)$, $L_2 = log\left(\frac{r-y'}{r+y'}\right)$ and $L_3 = log(r + z_1)$.

According to the superposition principle, this equation can now be used to calculate the total field anomaly at magnetometer position $i = 1,\ldots,n$ for the sample approximated by m voxels by summing over all voxels:

$$\begin{aligned}\Delta B_i = C_m \cdot \sum_{j=1}^{m} \{ & M_x [X(x_{2,j}, y_{2,j}, z_{top,j}) - X(x_{2,j}, y_{2,j}, z_{bottom,j}) \\ & + X(x_{1,j}, y_{1,j}, z_{top,j}) - X(x_{1,j}, y_{1,j}, z_{bottom,j}) + X(x_{1,j}, y_{2,j}, z_{bottom,j}) \\ & - X(x_{1,j}, y_{2,j}, z_{top,j}) + X(x_{2,j}, y_{1,j}, z_{bottom,j}) - X(x_{2,j}, y_{1,j}, z_{top,j})] \\ & + M_y [Y(x_{2,j}, y_{2,j}, z_{top,j}) - Y(x_{2,j}, y_{2,j}, z_{bottom,j}) + Y(x_{1,j}, y_{1,j}, z_{top,j}) \\ & - Y(x_{1,j}, y_{1,j}, z_{bottom,j}) + Y(x_{1,j}, y_{2,j}, z_{bottom,j}) - Y(x_{1,j}, y_{2,j}, z_{top,j}) \\ & + Y(x_{2,j}, y_{1,j}, z_{bottom,j}) - Y(x_{2,j}, y_{1,j}, z_{top,j})] \\ & + M_z [Z(x_{2,j}, y_{2,j}, z_{top,j}) - Z(x_{2,j}, y_{2,j}, z_{bottom,j}) + Z(x_{1,j}, y_{1,j}, z_{top,j}) \\ & - Z(x_{1,j}, y_{1,j}, z_{bottom,j}) + Z(x_{1,j}, y_{2,j}, z_{bottom,j}) - Z(x_{1,j}, y_{2,j}, z_{top,j}) \\ & + Z(x_{2,j}, y_{1,j}, z_{bottom,j}) - Z(x_{2,j}, y_{1,j}, z_{top,j})] \}\end{aligned} \tag{3}$$

with $X(x', y', z_1)$,$Y(x', y', z_1)$ and $Z(x', y', z_1)$ being the expressions in brackets behind the magnetization components in Equation 2.

The effect of the sample for induced magnetization ($\Delta B_{ind,i}$) can be calculated using Equation 3 with

$$\overrightarrow{M_{ind}} = \frac{\kappa \cdot |B_r|}{\mu_0 \cdot (1+\kappa)} \cdot \begin{pmatrix} cos(I) \cdot cos(D) \\ cos(I) \cdot sin(D) \\ sin(I) \end{pmatrix} = \begin{pmatrix} M_{x,ind} \\ M_{x,ind} \\ M_{z,ind} \end{pmatrix} \tag{4}$$

with κ being the magnetic susceptibility in SI, $|B_r| = 50000$ nT the intensity of the regional magnetic field, $\mu_0 = 4\pi \cdot 1e-7$ H/m the magnetic permeability in vacuum and I and D inclination and declination of the regional ambient magnetic field, respectively. Because the induced magnetization is independent of the rotation of the sample, except of time variations of $|B_r|$ and the non-equal rotational shape of the sample, it is assumed to be constant. This assumption will be evaluated during the discussion.

The inversion problem can now be written in the form

$$a = Kb \tag{5}$$

with

$$a = \Delta B_{obs} - \Delta B_{ind} = \Delta B_{rem} \text{ (column vector of length } n)$$

$$K = \begin{pmatrix} K_{x,1} & K_{y,1} & K_{z,1} \\ \dots & \dots & \dots \\ K_{x,n} & K_{y,n} & K_{z,n} \end{pmatrix} \text{ (matrix with } n \text{ rows and three columns)}$$

$$b = \begin{pmatrix} M_{x,rem} \\ M_{y,rem} \\ M_{z,rem} \end{pmatrix} \text{ (column vector of length 3)}$$

where ΔB_{ind} and ΔB_{rem} are the anomalous fields originating from induced and remanent magnetization, respectively. The coefficients in matrix K are calculated using Equation 3 as

$$\begin{aligned} K_{x,i} = \sum_{j=1}^{m} C_m \big[& X(x_{2,j}, y_{2,j}, z_{top,j}) - X(x_{2,j}, y_{2,j}, z_{bottom,j}) + X(x_{1,j}, y_{1,j}, z_{top,j}) \\ & - X(x_{1,j}, y_{1,j}, z_{bottom,j}) + X(x_{1,j}, y_{2,j}, z_{bottom,j}) \\ & - X(x_{1,j}, y_{2,j}, z_{top,j}) + X(x_{2,j}, y_{1,j}, z_{bottom,j}) \\ & - X(x_{2,j}, y_{1,j}, z_{top,j.}) \big] \end{aligned}$$

$$\begin{aligned} K_{y,i} = \sum_{j=1}^{m} C_m \big[& Y(x_{2,j}, y_{2,j}, z_{top,j}) - Y(x_{2,j}, y_{2,j}, z_{bottom,j}) + Y(x_{1,j}, y_{1,j}, z_{top,j}) \\ & - Y(x_{1,j}, y_{1,j}, z_{bottom,j}) + Y(x_{1,j}, y_{2,j}, z_{bottom,j}) \\ & - Y(x_{1,j}, y_{2,j}, z_{top,j}) + Y(x_{2,j}, y_{1,j}, z_{bottom,j}) \\ & - Y(x_{2,j}, y_{1,j}, z_{top,j}) \big] \end{aligned}$$

$$\begin{aligned} K_{z,i} = \sum_{j=1}^{m} C_m \big[& Z(x_{2,j}, y_{2,j}, z_{top,j}) - Z(x_{2,j}, y_{2,j}, z_{bottom,j}) + Z(x_{1,j}, y_{1,j}, z_{top,j}) \\ & - Z(x_{1,j}, y_{1,j}, z_{bottom,j}) + Z(x_{1,j}, y_{2,j}, z_{bottom,j}) \\ & - Z(x_{1,j}, y_{2,j}, z_{top,j}) + Z(x_{2,j}, y_{1,j}, z_{bottom,j}) \\ & - Z(x_{2,j}, y_{1,j}, z_{top,j}) \big] \end{aligned}$$

The over-determined linear system of Equation 5 can now be solved for b using least squares:

$$b = (K^T K)^{-1} K^T a. \tag{6}$$

The remanent magnetization vector can be reformulated to result in intensity M_{rem} as well as remanent inclination and declination (I_{rem} and D_{rem}) using

$$M_{rem} = \sqrt{M_{x,rem}^2 + M_{y,rem}^2 + M_{z,rem}^2} \tag{7}$$

$$I_{rem} = arcsin\left(\frac{M_{z,rem}}{M_{rem}}\right) (I_{rem} \in [-90, 90]) \tag{8}$$

$$D_{rem} = arccos\left(\frac{M_{x,rem}}{\sqrt{M_{x,rem}^2 + M_{y,rem}^2}}\right) (D_{rem} \in [-180, 180]) \tag{9}$$

A.2 | Set-up of the inversion problem using a sphere model

The magnetic field of a sphere with induced and remanent magnetization can be determined using

$$\vec{B} = C_m \cdot \frac{m}{r^3} \cdot [3(\hat{m} \cdot \hat{r})\hat{r} - \hat{m}] \tag{10}$$

with constant $C_m = 10^{-7}$ H/m, dipole moment $\vec{m} = m \cdot \hat{m}$, where $\hat{m}$ is the unit vector in the direction of the moment and m the magnitude of the moment, and $\vec{r} = r \cdot \hat{r}$, where $\hat{r} = (r_x; r_y; r_z)$ is the unit vector in the direction from the sphere to the measurement point and r the distance between measurement point and sphere (Blakely, 1996). The dipole moment is the product of the volume of the sphere V with the magnetization $\vec{M}$:

$$\vec{m} = V \cdot \vec{M} = \frac{4\pi \cdot radius^3}{3} \cdot \left(\overrightarrow{M_{ind}} + \overrightarrow{M_{rem}}\right) = V \cdot \left(\begin{bmatrix} M_{x,ind} \\ M_{y,ind} \\ M_{z,ind} \end{bmatrix} + \begin{bmatrix} M_{x,rem} \\ M_{y,rem} \\ M_{z,rem} \end{bmatrix}\right) \tag{11}$$

where the magnetization is the sum of induced ($\overrightarrow{M_{ind}}$) and remanent magnetization ($\overrightarrow{M_{rem}}$) and *radius* is the radius of the sphere. The induced magnetization is given by Equation 4 with

$$\left|\overrightarrow{M_{ind}}\right| = M_{ind}.$$

Again, the three unknown parameters to be determined during inversion are $M_{x,rem}$,$M_{y,rem}$ and $M_{z,rem}$. The total field anomaly of a sphere is calculated by the inner product of with the direction of the regional field given by the vector $[f_x; f_y; f_z] = [cos(I) \cdot cos(D); cos$

TABLE A1 Rotation angles around *x*- and *y*-axis and virtual measurement positions and induced magnetization angles for the 64 measurement positions

Position number	Rotational angle around *x*-axis (°)	Rotational angle around *y*-axis (°)	Virtual measurement position			Virtual induced magnetization angle	
			x (m)	*y* (m)	*z* (m)	Inclination (°)	Declination (°)
1[a]	0	0	0.245	0.000	−0.245	69.13	0.00
2[a,b]	0	45	0.000	0.000	−0.347	24.13	0.00
3[a]	0	90	−0.245	0.000	−0.245	−20.87	0.00
4[a,b]	0	135	−0.347	0.000	0.000	−65.87	0.00
5[a]	0	180	−0.245	0.000	0.245	−69.13	180.00
6[a,b]	0	225	0.000	0.000	0.347	−24.13	180.00
7[a]	0	270	0.245	0.000	0.245	20.87	180.00
8[a,b]	0	315	0.347	0.000	0.000	65.87	180.00
9	45	0	0.245	0.173	−0.173	41.35	−61.67
10[a]	45	45	0.000	0.245	−0.245	16.80	−17.58
11	45	90	−0.245	0.173	−0.173	−14.59	15.09
12	45	135	−0.347	0.000	0.000	−40.19	57.65
13	45	180	−0.245	−0.173	0.173	−41.35	118.34
14	45	225	0.000	−0.245	0.245	−16.80	162.42
15	45	270	0.245	−0.173	0.173	14.59	−164.91
16	45	315	0.347	0.000	0.000	40.19	−122.35
17[a]	90	0	0.245	0.245	0.000	0.00	−69.13
18[a,b]	90	45	0.000	0.347	0.000	0.00	−24.13
19[a]	90	90	−0.245	0.245	0.000	0.00	20.87
20[a]	90	135	−0.347	0.000	0.000	0.00	65.87
21[a]	90	180	−0.245	−0.245	0.000	0.00	110.87
22[a]	90	225	0.000	−0.347	0.000	0.00	155.87
23[a]	90	270	0.245	−0.245	0.000	0.00	−159.13
24[a]	90	315	0.347	0.000	0.000	0.00	−114.13
25	135	0	0.245	0.173	0.173	−41.35	−61.67
26[a]	135	45	0.000	0.245	0.245	−16.80	−17.58
27	135	90	−0.245	0.173	0.173	14.59	15.09
28	135	135	−0.347	0.000	0.000	40.19	57.65
29	135	180	−0.245	−0.173	−0.173	41.35	118.34
30	135	225	0.000	−0.245	−0.245	16.80	162.42
31	135	270	0.245	−0.173	−0.173	−14.59	−164.91
32	135	315	0.346	0.000	0.000	−40.19	−122.35
33	180	0	0.245	0.000	0.245	−69.13	0.00
34[a]	180	45	0.000	0.000	0.347	−24.13	0.00
35	180	90	−0.245	0.000	0.245	20.87	0.00
36	180	135	−0.346	0.000	0.000	65.87	0.00
37	180	180	−0.245	0.000	−0.245	69.13	180.00
38	180	225	0.000	0.000	−0.347	24.13	180.00
39	180	270	0.245	0.000	−0.245	−20.87	180.00
40	180	315	0.346	0.000	0.000	−65.87	180.00
41	225	0	0.245	−0.173	0.173	−41.35	61.67
42[a]	225	45	0.000	−0.245	0.245	−16.80	17.58
43	225	90	−0.245	−0.173	0.173	14.59	−15.09
44	225	135	−0.346	0.000	0.000	40.19	−57.65

(Continues)

TABLE A1 (Continued)

Position number	Rotational angle around x-axis (°)	Rotational angle around y-axis (°)	Virtual measurement position			Virtual induced magnetization angle	
			x (m)	y (m)	z (m)	Inclination (°)	Declination (°)
45	225	180	−0.245	0.173	−0.173	41.35	−118.33
46	225	225	0.000	0.245	−0.245	16.80	−162.42
47	225	270	0.245	0.173	−0.173	−14.59	164.91
48	225	315	0.346	0.000	0.000	−40.19	122.36
49	270	0	0.245	−0.245	0.000	0.00	69.13
50[a,b]	270	45	0.000	−0.347	0.000	0.00	24.13
51	270	90	−0.245	−0.245	0.000	0.00	−20.87
52	270	135	−0.346	0.000	0.000	0.00	−65.87
53	270	180	−0.245	0.245	0.000	0.00	−110.87
54	270	225	0.000	0.347	0.000	0.00	−155.87
55	270	270	0.245	0.245	0.000	0.00	159.13
56	270	315	0.346	0.000	0.000	0.00	114.13
57	315	0	0.245	−0.173	−0.173	41.35	61.67
58[a]	315	45	0.000	−0.245	−0.245	16.80	17.58
59	315	90	−0.245	−0.173	−0.173	−14.59	−15.09
60	315	135	−0.346	0.000	0.000	−40.19	−57.65
61	315	180	−0.245	0.173	0.173	−41.35	−118.33
62	315	225	0.000	0.245	0.245	−16.80	−162.42
63	315	270	0.245	0.173	0.173	14.59	164.91
64	315	315	0.346	0.000	0.000	40.19	122.35

Note: The declination for the starting position is 0° because the *x*-axis was directed towards magnetic north.
[a]These positions were used for the reduced dataset with 22 points.
[b]These positions were used for the reduced dataset with six points.

$(I) \cdot sin(D)$; $sin(I)]$ and is linearly depending on the three unknown parameters:

$$\begin{aligned}\Delta B = {} & M_{x,rem} \cdot C_m \cdot \frac{V}{r^3} \cdot \left(f_x \cdot \left(3r_x^2 - 1\right) + f_y \cdot 3r_x r_y + f_z \cdot 3r_x r_z\right) \\ & + M_{y,rem} \cdot C_m \cdot \frac{V}{r^3} \cdot \left(f_x \cdot 3r_x r_y + f_y \cdot \left(3r_y^2 - 1\right) + f_z \cdot 3r_y r_z\right) \\ & + M_{z,rem} \cdot C_m \cdot \frac{V}{r^3} \cdot \left(f_x \cdot 3r_x r_z + f_y \cdot 3r_y r_z + f_z \cdot \left(3r_z^2 - 1\right)\right) \\ & + M_{ind} \cdot C_m \cdot \frac{V}{r^3} \cdot \left(f_x \cdot \left[3f_x r_x^2 + 3f_y r_y r_x + 3f_z r_z r_x - f_x\right]\right. \\ & + f_y \cdot \left[3f_x r_x r_y + 3f_y r_y^2 + 3f_z r_z r_y - f_y\right] \\ & \left. + f_z \cdot \left[3f_x r_x r_z + 3f_y r_y r_z + 3f_z r_z^2 - f_z\right]\right)\end{aligned} \quad (12)$$

And therefore for $i = 1,\ldots,n$ measurements

$$\Delta B_i = M_{x,rem} \cdot K_{x,i} + M_{y,rem} \cdot K_{y,i} + M_{z,rem} \cdot K_{z,i} + \Delta B_{ind,i} \quad (13)$$

with $K_{x,i}$, $K_{y,i}$ and $K_{z,i}$ being the factors behind the unknown parameters in Equation 12.

Similar to the inversion problem using voxels, an over-determined set of linear equations of the form of Equation 5 can be assembled with

$$a = \Delta B_{obs} - \Delta B_{ind} \text{ (column vector of length } n\text{)}$$

$$K = \begin{pmatrix} K_{x,1} & K_{y,1} & K_{z,1} \\ \ldots & \ldots & \ldots \\ K_{x,n} & K_{y,n} & K_{z,n} \end{pmatrix} \text{ (matrix with } n \text{ rows and three columns)}$$

$$b = \begin{pmatrix} M_{x,rem} \\ M_{y,rem} \\ M_{z,rem} \end{pmatrix} \text{ (column vector of length 3)}$$

where the components of K correspond to the coefficients in Equation 13. Again, the linear system of equations is solved using least squares.

TABLE A2 List of all results for all five samples

Sample #	Pos.	I_{rem} (°)	D_{rem} (°)	M_{rem} (A/m)	Offset (nT)	RMS (nT)	Geometry
10067	63	54.02	18.44	1.75	0.29	0.26	V 5 mm
		54.02	18.44	1.75	0.29	0.26	V 2.5 mm
		54.04	18.45	1.76	0.30	0.26	Sphere
	21	43.32	23.60	1.71	0.30	0.45	V 5 mm
		43.31	23.60	1.72	0.30	0.45	V 2.5 mm
		42.98	23.76	1.72	0.30	0.45	Sphere
	6	44.81	14.25	1.81	0.28	0.46	V 5 mm
		44.79	14.27	1.81	0.28	0.46	V 2.5 mm
		44.67	15.29	1.85	0.27	0.47	Sphere
10070	63	−16.74	118.50	0.95	0.66	0.16	V 5 mm
		−16.74	118.50	0.94	0.66	0.16	V 2.5 mm
		−16.63	118.90	0.94	0.68	0.18	Sphere
	22	−13.79	124.33	0.89	0.68	0.69	V 5 mm
		−13.79	124.35	0.89	0.68	0.69	V 2.5 mm
		−13.27	125.29	0.88	0.69	0.71	Sphere
	6	−19.49	129.97	0.70	0.64	0.72	V 5 mm
		−19.51	130.03	0.70	0.64	0.72	V 2.5 mm
		−20.62	132.61	0.69	0.65	0.74	Sphere
10071	64	14.57	166.43	1.55	0.57	0.16	V 5 mm
		14.57	166.42	1.54	0.57	0.16	V 2.5 mm
		14.70	166.41	1.52	0.57	0.17	Sphere
	22	20.49	173.94	1.62	0.53	0.60	V 5 mm
		20.51	173.95	1.61	0.53	0.60	V 2.5 mm
		19.65	174.04	1.58	0.53	0.61	Sphere
	6	23.57	168.48	1.62	0.52	0.60	V 5 mm
		23.58	168.55	1.60	0.52	0.60	V 2.5 mm
		22.91	170.63	1.54	0.52	0.61	Sphere
10072	64	54.91	−1.41	3.22	0.70	0.56	V 5 mm
		54.91	−1.40	3.21	0.70	0.56	V 2.5 mm
		54.77	−1.18	3.15	0.68	0.57	Sphere
	22	44.83	7.56	3.03	0.67	1.03	V 5 mm
		44.82	7.56	3.03	0.67	1.03	V 2.5 mm
		43.76	7.26	2.93	0.64	1.04	Sphere
	6	41.93	3.61	3.18	0.59	1.11	V 5 mm
		41.95	3.56	3.17	0.59	1.11	V 2.5 mm
		42.40	4.17	3.17	0.59	1.10	Sphere
10073	64	8.37	−18.59	1.72	0.53	0.24	V 5 mm
		8.38	−18.59	1.72	0.53	0.24	V 2.5 mm
		8.32	−18.31	1.67	0.51	0.25	Sphere
	22	−1.42	−5.35	1.79	0.55	0.62	V 5 mm
		−1.44	−5.36	1.79	0.55	0.62	V 2.5 mm
		−1.23	−5.49	1.76	0.54	0.61	Sphere
	6	−4.10	−4.22	1.79	0.54	0.63	V 5 mm
		−4.11	−4.23	1.79	0.54	0.64	V 2.5 mm
		−2.82	−4.33	1.75	0.54	0.61	Sphere

Notes: From the directly inverted parameters $M_{x,rem}$, $M_{y,rem}$ and $M_{z,rem}$, the magnetization and direction of the NRM are derived. V *mm stands for voxel with *mm edge length.